ORIGINAL PAPER

Unstructured polygonal meshes with adaptive refinement for the numerical simulation of dynamic cohesive fracture

**Daniel W. Spring · Sofie E. Leon ·
Glaucio H. Paulino**

Abstract This paper presents a scheme for adaptive mesh refinement on unstructured polygonal meshes to better capture crack patterns in dynamic cohesive fracture simulations. A randomly seeded polygonal mesh leads to an isotropic discretization of the problem domain, which does not bias crack patterns, but restricts the number of paths that a crack may travel at each node. An adaptive refinement scheme is proposed and investigated through a detailed set of geometric studies. The refinement scheme is selectively chosen to optimize the number of paths that a crack may travel, while still maintaining a conforming domain discretization. The details of the refinement scheme are outlined, along with the criterion used to determine the region of refinement and the method of interpolating nodal attributes. Extrinsic cohesive elements are inserted when and where necessary, and follow the constitutive response of the Park–Paulino–Roesler cohesive model. The influence of bulk and cohesive material heterogeneity is investigated through the use of a statistical distribution of material properties. The adap-

tive mesh modifications are handled through a compact topological data structure. Numerical examples highlight the features of adaptive refinement in capturing physical fracture patterns while addressing computational cost. Thus, the present approach is a step towards obtaining accurate dynamic fracture patterns and fields with polygonal elements.

1 Introduction

Adaptive mesh refinement schemes have been used to both reduce error in finite element analysis, and to reduce computational cost (Babuška and Rheinboldt 1978; Paulino et al. 1999; Grätsch and Klaus-Jürgen 2005). In large scale simulations, in order to capture multiscale effects, fine meshes are used around regions of high stress and strain gradients, and coarse meshes are used far from these regions (Park et al. 2012). In dynamic fracture simulations, the region in the vicinity of the propagating crack tip has high stress and strain gradients and thus requires a fine mesh. Instead of prescribing a fine mesh in the region of expected fracture propagation, an adaptive refinement scheme allows for the unrestricted dynamic propagation of the crack. This approach has been applied by many researchers: Molinari and Ortiz (2002) developed an adaptive refine-

D. W. Spring · S. E. Leon · G. H. Paulino (✉)
Department of Civil and Environmental Engineering,
University of Illinois at Urbana-Champaign, 205 North
Mathews Ave., Urbana, IL 61801, USA
e-mail:paulino@illinois.edu

D. W. Spring
e-mail:spring2@illinois.edu

S. E. Leon
e-mail:leon7@illinois.edu

ment technique based on Rivara's longest edge propagation path bisection algorithm; Park et al. (2012) presented a multilevel refinement and coarsening strategy for 4k meshes in the simulation of dynamic fracture problems; Khoei et al. (2008) investigated crack propagation using adaptive mesh refinement based on a modified super-convergent patch recovery technique (Zienkiewicz and Zhu 1992a, b).

Popular means of modeling dynamic fracture problems are based on the finite element method (FEM) and the extended/generalized finite element method (XFEM/GFEM) (Belytschko and Black 1999; Strouboulis et al. 2000, 2001). The XFEM/GFEM approach uses local enrichment functions to capture discontinuous fields across a crack. The discontinuous nature of the enrichment functions presents difficulties for both numerical integration (Park et al. 2009) and time stepping algorithms (Remmers et al. 2008; Fries and Zilian 2009). In addition, the means by which the XFEM/GFEM approach models crack branching and crack coalescence, especially in three-dimensions, can become prohibitively complex (Bishop 2009). Alternatively, in the standard finite element framework, cohesive zone elements (CZEs) can be used to represent the inelastic region in front of the crack tip. The CZEs are inserted between bulk elements, and initially have zero thickness. As the bulk elements separate, signifying fracture, the cohesive elements impart a traction on the adjacent bulk elements; which corresponds to a specified cohesive zone model. "Intrinsic cohesive zone elements" are inserted a priori into a mesh and have a traction-separation relation which consists of both an initial elastic range and a softening range (Zhang and Paulino 2005; Cerrone et al. 2014). This initial elastic range creates an artificial compliance in the mesh and can lead to non-physical results (Klein et al. 2000; Blal et al. 2012). On the other hand, "extrinsic cohesive zone elements" can be inserted adaptively into the mesh (Ortiz and Pandolfi 1999; Zhang et al. 2007). The traction–separation relation, corresponding to an extrinsic cohesive zone model, only consists of a softening range and thus does not cause artificial compliance.

Previously proposed adaptive refinement schemes, for two-dimensional dynamic fracture simulations, have used a 4k mesh structure (Park et al. 2012; Velho and Gomes 2000). The 4k mesh structure us composed of regular isosceles triangles with 45° interior angles (see, for example, Figure 1 in Park et al. 2012). Adaptive refinement using the 4k mesh structure has shown great promise. Since, in this case, the refined mesh is also a 4k structure, a systematic procedure of refinement can be developed for one level of refinement which then translates directly to the next level. By keeping track of the levels of refinement, an analogous coarsening scheme can be applied. The drawback of using a 4k mesh is that it might lead to an anisotropic discretization of the problem domain (Rimoli et al. 2012; Rimoli and Rojas 2013). The 4k mesh is ideal for modeling cracks which propagate at angles that are a multiple of 45°, but presents mesh-induced geometric errors when modeling crack paths which deviate greatly from these angles (Rimoli et al. 2012). To minimize this effect, edge-swap and nodal perturbation operators were introduced to make the mesh topologically and geometrically unstructured (Paulino et al. 2010). However, the unstructured 4k mesh has been shown to only moderately reduce, not remove, the effect of anisotropy (Rimoli et al. 2012). In order to overcome such pathology, unstructured polygonal meshes are proposed, as discussed below.

There are many commonly encountered examples where we see polygonal shaped crack patterns, as illustrated in Fig. 1. A nice feature of unstructured polygonal meshes, and the primary focus in this work, is that they show no preference to crack propagation directions. These meshes have been used by many researchers to study fracture. In 1996, Li and Ghosh (2006a, b) used polygonal meshes within the XFEM framework to model multiple crack growth. They were able to capture crack coalescence phenomena by assuming a pre-existing crack within each element of the mesh. Bolander and Saito (1998) used a rigid-body-spring network, at the interfaces of a polygonal mesh, to study the fracture of homogeneous isotropic solids. Later, Hu and Ghosh (2008) used polygonal meshes to model plastic strain-induced softening in the ductile failure of heterogeneous metals and alloys. Bishop (2009) and Bishop et al. (2012) applied random polygonal meshes with CZEs to model pervasive fracture of materials and structures. While many of these investigations have shown great promise, they are all based on the use of a geometrically static mesh. Recently, Ooi et al. (2012a, 2013) have proposed using dynamic (adaptively refined) meshes to model propagating cracks in polygonal meshes using a scaled boundary finite ele-
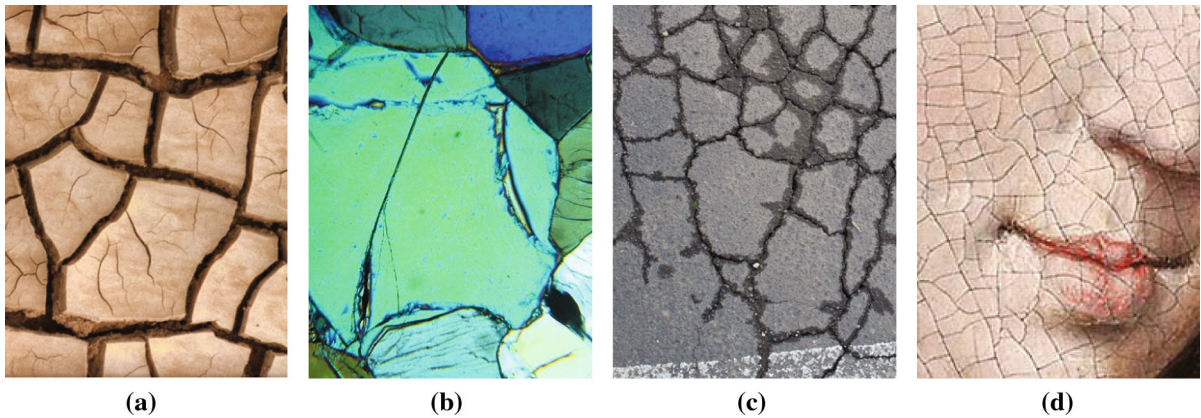
Fig. 1 Common examples where cracking displays polygonal shaped patterns: **a** mud flats after drying (www.freebiewebresources.com), **b** intergranular and intragranular cracking (http://www.und.nodak.edu), **c** crocodile cracking in asphalt (en.wikipedia.org), and **d** paint chipping after aging (www-hki.fitzmuseum.cam.ac.uk)

ment method; allowing them to solve problems with relatively coarse domains.

In this paper, we use an adaptive refinement technique to refine the region in front of a propagating crack tip during dynamic cohesive fracture simulations in two-dimensions. The mesh is unstructured and the refinement technique is conforming. Away from the crack tip, a coarse mesh is used. In addition to adaptive refinement, adaptive element splitting (Leon et al. 2014) is used to improve the path convergence characteristics of the polygonal mesh. The adaptive qualities of the mesh are handled with a compact and efficient topological data structure called TopS (Celes et al. 2005a, b). The cohesive elements are inserted on the fly, where and when needed, and follow the constitutive response of the extrinsic Park–Paulino–Roesler (PPR) cohesive model (Park et al. 2009). The remainder of the paper is organized as follows. Section 2 outlines the generation of unstructured polygonal meshes and the refinement scheme proposed in this work. In Sect. 3, we present a series of geometric studies which quantify the improvements that refinement has on the ability of a mesh to capture fracture behavior. In Sect. 4, we briefly discuss the constitutive models and the incorporation of material randomness in homogeneous materials. Numerical examples are presented in Sect. 5; which highlight the advantages of adaptive refinement in both capturing physical fracture phenomena and decreasing computational cost. Finally, our conclusions are presented in Sect. 6.

2 Adaptive refinement of unstructured polygonal meshes

The unstructured polygonal meshes in this work are generated using the PolyMesher algorithm (Talischi et al. 2012), which discretizes a domain with a centroidal Voronoi tessellation (CVT). The details for generating these tessellations can be found in the principal publication; we just highlight a few critical details for completeness, and maintain the notation of Talischi et al. (2012) for consistency. Briefly, to initiate the tessellation, a random set of seeds are inserted into the problem domain. The number of seeds corresponds to the number of elements chosen to discretize to the domain. Given a set of seeds, $\mathbf{P}$, the Voronoi tessellation, $\mathcal{T}$, of the domain, Ω, is defined as:

$$\mathcal{T}(\mathbf{P}; \Omega) = \left\{ V_{\mathbf{y}} \cap \Omega : \mathbf{y} \in \mathbf{P} \right\} \tag{1}$$

where $V_{\mathbf{y}}$ is the Voronoi cell corresponding to point $\mathbf{y}$. The Voronoi cell consists of all points in the domain which are closer to $\mathbf{y}$ than to any other point in the set $\mathbf{P}$:

$$V_{\mathbf{y}} = \{\mathbf{x} \in \Omega : \|\mathbf{x} - \mathbf{y}\| < \|\mathbf{x} - \mathbf{z}\|, \forall \mathbf{z} \in \mathbf{P} \backslash \{\mathbf{y}\}\}. \tag{2}$$

The initial discretization, based off the initial set of seeds, results in a random polygonal mesh, as illustrated in Fig. 2a. In dynamic fracture simulations, the time step required to produce a stable simulation is dependent on the element size (Remmers et al. 2008). Because the random placement of seeds may result
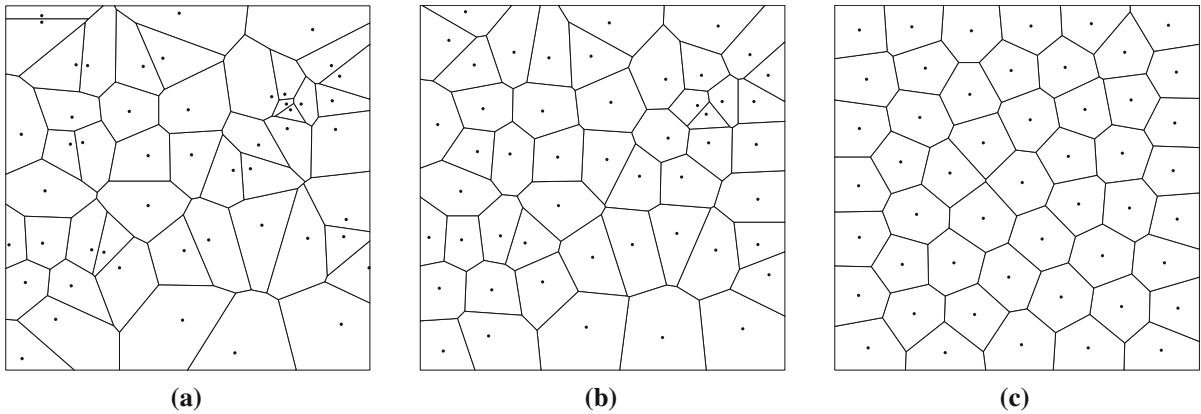
Fig. 2 Initial placement of seeds and the corresponding Voronoi tessellation. **a** Voronoi Tessellation after first iteration of Lloyd's algorithm, and **b** final Voronoi tessellation Talischi et al. (2012)

Fig. 3 Local geometry in an arbitrary n-gon, **a** prior to refinement (with original connectivity), and **b** after refinement with quadrilaterals, **c** connectivity in a refined element
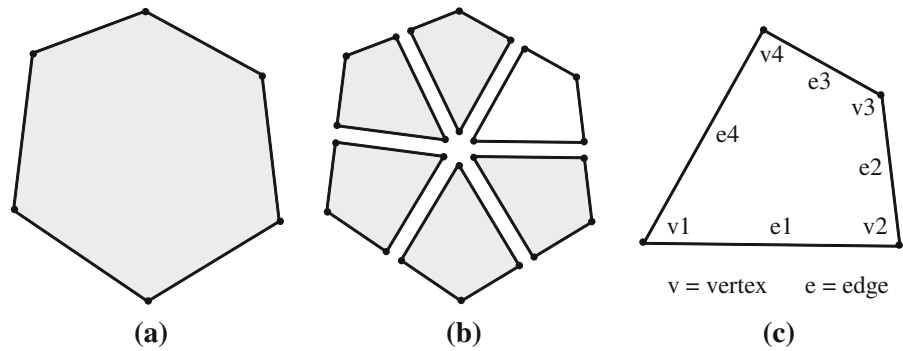
in arbitrarily small elements and/or element edges, this initial discretization is not suitable for simulation of dynamic fracture. To improve the quality of the mesh, Lloyd's iterative updating algorithm is employed (Lloyd 1982). It generates a new set of seeds at every iteration, based on the previous Voronoi tessellation. The new locations of the seeds correspond to the centroidal location of each Voronoi cell in the previous tessellation. Figure 2b shows the resulting Voronoi tessellation after one update using Lloyd's algorithm on the random seeds in Fig. 2a. This updating process continues until the change in the energy of the tessellation, from one iteration to the next, falls below a selected tolerance (Talischi et al. 2012). The resulting tessellation after 50 iterations of Lloyd's algorithm is illustrated in Fig. 2c. The resulting mesh is more uniform, and is thus more suitable for use in simulating dynamic fracture problems. An investigation of mesh quality will be presented in Sect. 3.

2.1 Refinement methodology

The refinement scheme we propose decomposes an n-sided polygon into n non-overlapping quadrilateral elements, as illustrated in Fig. 3. To conduct the refinement within each element, we need to determine the location of the centroid of the n-gon. First, the signed area of the n-gon is calculated based on the physical coordinates of its vertices:

$$A = \frac{1}{2} \sum_{k=1}^{n} \left(v_x^{[k]} v_y^{[k+1]} - v_x^{[k+1]} v_y^{[k]} \right) \tag{3}$$

where $(v_x^{[k]}, v_y^{[k]})$ is the coordinates of the kth vertex of the n-gon, $k = 1, \ldots, n$, and the $(n + 1)$th vertex is assumed to be the 1st vertex. From the area, the geometric location of the centroid (c_x, c_y) is calculated as follows:

$$c_x = \frac{1}{6A} \sum_{k=1}^{n} \left(v_x^{[k]} + v_x^{[k+1]} \right) \left(v_x^{[k]} v_y^{[k+1]} - v_x^{[k+1]} v_y^{[k]} \right),$$

(4)

$$c_y = \frac{1}{6A} \sum_{k=1}^{n} \left(v_y^{[k]} + v_y^{[k+1]} \right) \left(v_x^{[k]} v_y^{[k+1]} - v_x^{[k+1]} v_y^{[k]} \right).$$

(5)

We then insert nodes at the centroid and the midpoints of the edges, see Fig. 3b. The original polygon is removed and replaced with quadrilateral elements connected at the centroid, one vertex of the original polygon, and the midpoints of the two adjacent edges. The resulting nodal connectivities are illustrated in Fig. 3c.

When nodes are added to the model, their attributes need to be initialized. Since we are using linear polygonal elements, the interpolation of nodal attributes is relatively straight forward.
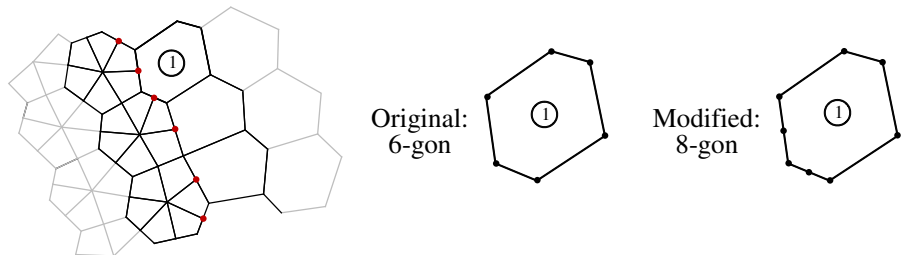
2.2 Interpolation scheme

There are several polygonal interpolants available in the literature, see, for example, the review paper by Sukumar (2006). Here, we adopt the Wachspress shape functions (Wachspress 1975). The centroidal nodal attributes, u_j^c, are interpolated from those of the original nodes of the n-gon using Wachspress shape functions. The interpolation takes the form:

$$u_j^c = \sum_{i=1}^{n} N_i(\boldsymbol{\xi}) u_i$$

(6)

where n is the number of vertices in the original n-gon, N_i are the Wachspress shape functions defined on a parent domain, $\boldsymbol{\xi}$ is an interior point in the n-gon, and u_i are the attributes to be interpolated. The centroid of the n-gon, in the parent domain, is $\boldsymbol{\xi} = (0, 0)$. The Wachspress shape functions are expressed as:

$$N_i(\boldsymbol{\xi}) = \frac{\alpha_i(\boldsymbol{\xi})}{\sum_{j=1}^{n} \alpha_j(\boldsymbol{\xi})}.$$

(7)

where α_i are interpolants of the form:

$$\alpha_i(\xi) = \frac{A(\mathbf{p}_{i-1}, \mathbf{p}_i, \mathbf{p}_{i+1})}{A(\mathbf{p}_{i-1}, \mathbf{p}_i, \boldsymbol{\xi}) A(\mathbf{p}_i, \mathbf{p}_{i+1}, \boldsymbol{\xi})}$$

(8)

where A denotes the area of the triangle made up of the points in its arguments Talischi et al. (2012). For the nodes which are added to the midpoints of the edges, the nodal attributes, u_j^m, are interpolated from the two adjacent nodes on the edge. In this case, the interpolation takes the form:

$$u_j^m = \sum_{i=1}^{2} \frac{1}{2} u_i$$

(9)

where u_i are the attributes to be interpolated. In this work, we use a bulk constitutive relation in which the material state is defined completely by the displacement vector, thus, only the displacement (a nodal quantity) needs to be mapped. If a constitutive relation which included rate or history effects were to be employed, it would be necessary to map internal state variables from the original integration points to the new ones (Mota et al. 2013); however, this is outside the scope of the current work.

Because nodes are added to the midpoints of the edges, the nodes are initially left hanging, as illustrated in Fig. 4. To account for this, all adjacent elements are modified to connect to the midpoint, resulting in three colinear nodes in each of these adjacent elements. The elements with colinear nodes remain convex (although not strictly), a condition which enables these elements to be handled naturally by the Wachspress shape functions. The refinement does not increase the minimum number of paths a crack may travel at the original nodes; however, the inserted midside nodes have four potential fracture paths (see Fig. 5), and the centroid nodes have n potential fracture paths. In order to increase the number of fracture paths at each node,

Fig. 4 Hanging nodes adjacent to region refined with quadrilateral elements and the subsequent modifications to the coincident edges of adjacent elements

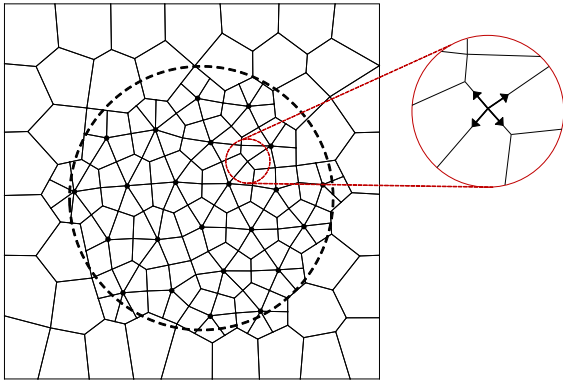Original: 6-gon

Modified: 8-gon

Fig. 5 Circular zone of refinement and corresponding refined mesh. The detail illustrates a typical midside node with the four potential paths on which a crack could propagate

we allow elements to be split, using the element splitting algorithm proposed by Leon et al. (2014).

Element splitting We employ the element-splitting technique introduced in reference Leon et al. (2014) to increase the possible fracture paths at element vertices and to reduce mesh bias. In the element splitting algorithm, an element can be split along any two nodes that minimize the difference between the areas of the resulting split elements. This restriction limits the occurrence of elements with small edges; which adversely effect the critical time step in a conditionally stable explicit time integration scheme.

When combined with the refinement scheme, elements are always refined before splitting is performed. Thus, restricting the direction in which elements can be split is not necessary, because there is only one possible direction for quadrilateral elements to be split. With the combined refinement and element splitting enabled, there are a total of $3n$ possible facets for cracks to prop-

agate along, within an original element, as illustrated in Fig. 6.

2.3 Refinement criteria

The simulation of dynamic fracture problems results in a propagating crack tip, as illustrated in Fig. 7. The mesh refinement procedure is conducted in an adaptive manner in a circular region around the propagating crack tip, as illustrated in Fig. 5. The influence of the radius of refinement is investigated further in Sect. 5.1. If the centroid of an element falls within the circular region, the element is refined. When refined with quadrilateral elements, the element splitting procedure is used to implicitly allow fracture paths to split elements in this region, but does not increase the number of "explicit edges" in the model. An explicit edge is an edge which is represented geometrically (as opposed to an intrinsic edge, which is only represented topologically, as in the element splitting method). In addition, the refinement scheme leaves nodes hanging at the boundaries of the circular region. To rectify these hanging nodes, the elements immediately outside the region of refinement are modified to have three co-linear nodes along those coincident edges, as discussed in the previous section.

3 Geometric investigation of refinement scheme

A desirable finite element mesh for fracture applications is isotropic; meaning the crack patterns are not biased by element orientation. Similarly, the mesh should be able to represent an arbitrary crack path, along the facets of the elements, without imposing large errors in the length of, and deviation from, the path. In
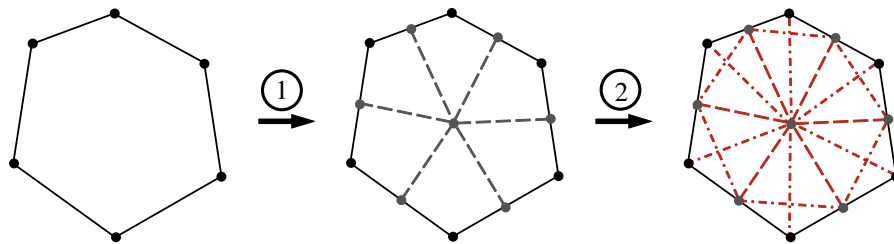

Fig. 6 Possible facets for fracture, progression for arbitrary n-gon (here 6-gon). Step 1: refinement (explicit facets) to introduce n possible facets for fracture within the element. Step 2: element splitting (implicit facets) to introduce $3n$ possible facets for fracture within the element
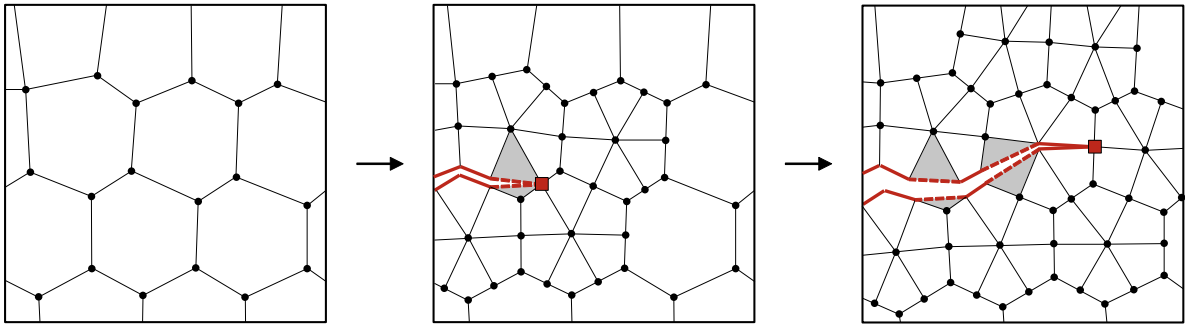
Fig. 7 Schematic illustrating the adaptive refinement scheme and a possible crack path propagating along both refined edges and split element edges

Fig. 8 Path length study, illustrating the shortest computed path (using Djikstra's shortest path algorithm) for **a** a polygonal mesh, and **b** a refined mesh. For visual clarity, the meshes illustrated here are much coarser than those used in the studies

(a)

(b)
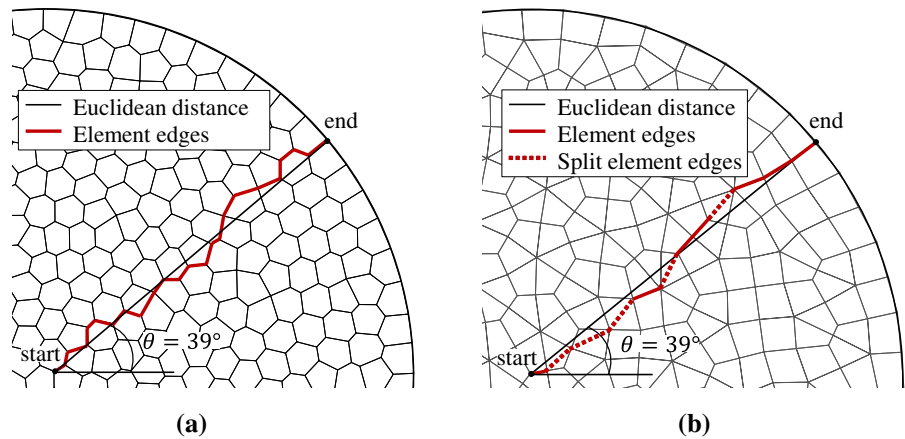
this section, we perform two geometric studies, similar to those proposed by Rimoli et al. (2012) and Leon et al. (2014), to investigate the quality of polygonal element meshes with adaptive refinement for fracture applications.

In the first study, we attempt to represent a straight line along the facets of a finite element mesh. Given a start and end point, we measure the shortest distance along the finite element facets using Djikstra's shortest path algorithm Dijkstra (1959), as illustrated in Fig. 8. The error in length (E_{length}) is quantified as the difference between the length along the element facets and the Euclidean distance between the start and end points. We perform this study on a circle of radius 1, centered on the origin. The start point is located at $(0, 0)$ and the end point at $(\cos\theta, \sin\theta)$, where $\theta = 0°, 1°, 2°, \ldots, 359°$. Desirable finite element meshes are those which have a small E_{length} and are isotropic, meaning that E_{length} is similar for all θ.

In the second geometric study, we quantify the deviation of the path along the element facets from the

straight line, using the Hausdorff distance (Huttenlocher et al. 1993; Rockafellar et al. 1998). Given two curves, P and Q the Hausdorff distance, H, is the maximum of the minimum distances from all points on curve P, denoted p, to all points on curve Q, denoted q. It is defined as Rockafellar et al. (1998):

$$H(P, Q) = \max(h(P, Q), h(Q, P)), \tag{10}$$

where

$$h(P, Q) = \max\left[\min_{p \in P}\left[\operatorname{dist}_{q \in Q}(p, q)\right]\right]. \tag{11}$$

Using the same circular domain as in the first study, we find the path along the element facets in which the angle between the start and end point is closest to the target angle ($\theta = 0°, 1°, 2°, \ldots, 359°$). To obtain the path, we perform a local search on the nodes adjacent to the start node and compute the angles between the adjacent nodes and $(0, 0)$. The adjacent node that results in an angle closest to the target angle is selected as the new
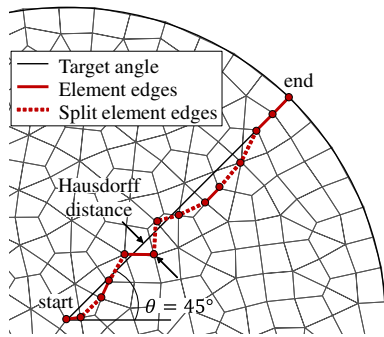
Fig. 9 Hausdorff distance study, illustrating the Hausdorff distance for a fracture path, along a refined mesh, with an angle of 45°. For visual clarity, the mesh illustrated here is much coarser than those used in the studies

start node. We continue until we reach the boundary of the mesh, as illustrated in Fig. 9. The error ($E_{Hausdorff}$) is simply the Hausdorff distance between the computed finite element path and the Euclidean path between the start point (0, 0) and end point ($\cos\theta$, $\sin\theta$).

To investigate the effect of mesh refinement, we first examine three mesh types: (1) coarse polygonal meshes of 1,700 elements each (we will refer to these as the coarse meshes), (2) the coarse meshes are uniformly refined with the refinement scheme proposed in Sect. 2 (we will refer to these as the uniformly refined meshes), (3) fine polygonal meshes where the number of polygonal elements in each mesh is equal to the number of elements in each of the uniformly refined meshes (we will refer to these as the fine meshes). Since the meshes are random, we generate 10 of each type of mesh and

present the averaged results. It is useful to note that CVTs, such as the ones used in this study, typically result in an average of 6 edges per element Talischi et al. (2012). Thus, the number of elements in a uniformly refined mesh which starts with 1,700, will be roughly 10,200. The results of the studies on length and deviation are illustrated in Figs. 10 and 11. We present the data in two graphical representations. First, the average and standard deviation of E_{length} and $E_{Hausdorff}$ at each angle are illustrated in Figs. 10a and 11a, respectively. From these plots it is clear that the meshes are isotropic, as there are no angles for which the error is significantly greater than or less than any other. The data is also illustrated in the form of a histogram in Figs. 10b and 11b in order to clearly display the distributions of the errors.

As illustrated in Fig. 10, the errors (E_{length}) present for the coarse meshes and fine meshes are similar. The average error for the fine meshes is slightly lower, with a slightly smaller standard deviation than that of the coarse meshes. Since the difference between the coarse and fine meshes is restricted to the number of polygonal elements in each (the fine meshes have approximately 6 times more elements than the coarse meshes), we see that the level of mesh refinement does not have a significant impact on the ability of a polygonal mesh to represent a straight line. However, when the quadrilateral refinement scheme is introduced, the error significantly reduces from 18–22 to 6–8 %. Although the error is significantly reduced, the standard deviations remain similar to that of coarse meshes, as illustrated in Fig. 10a.
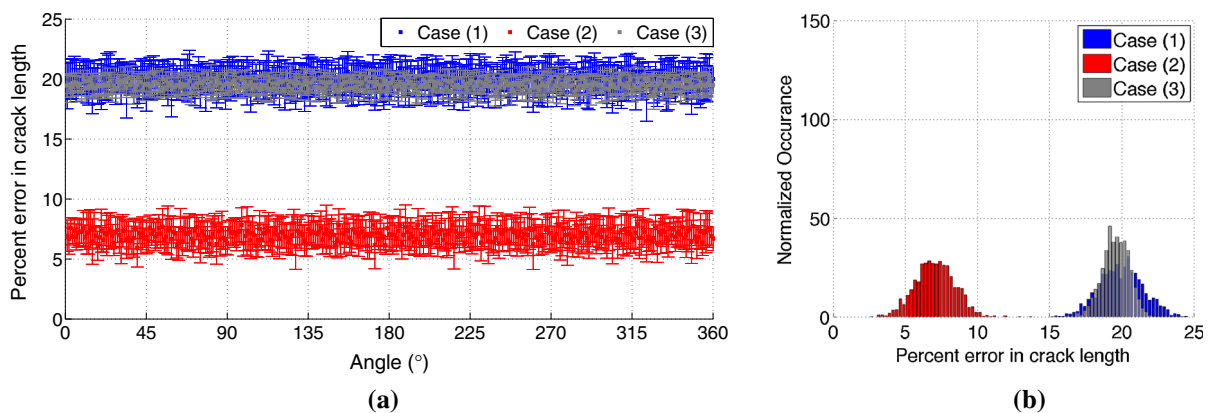

Fig. 10 Error in crack length, E_{length} for Case 1, coarse meshes; Case 2, uniformly refined meshes; and Case 3, fine meshes. **a** Cartesian representation shows the average E_{length} over 10 meshes for each angle with band representing the standard deviation, and **b** histogram representation
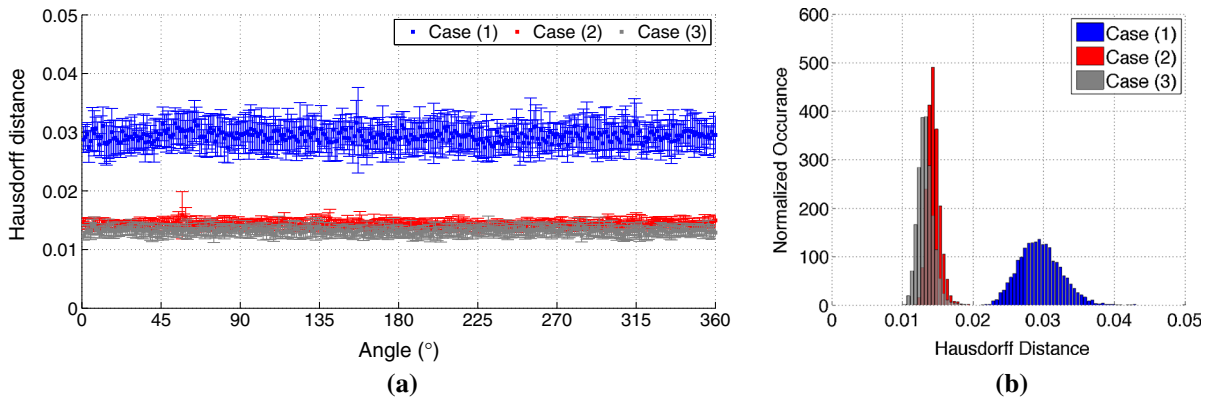
Fig. 11 Hausdorff distances, $E_{\text{Hausdorff}}$ for Case 1, coarse meshes; Case 2, uniformly refined meshes; and Case 3, fine meshes. **a** Cartesian representation shows the average $E_{\text{Hausdorff}}$ over 10 meshes for each angle with band representing the standard deviation, and **b** histogram representation
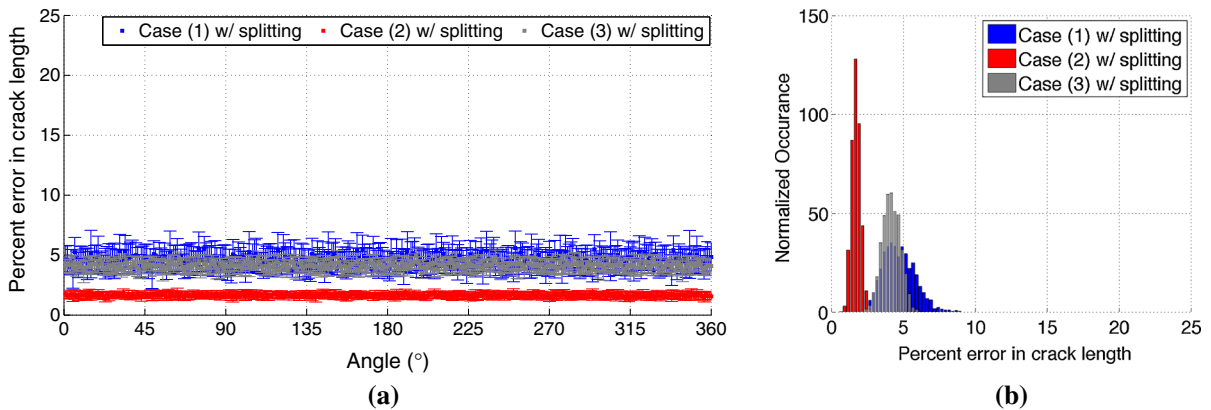

Fig. 12 Error in crack length, E_{length} for Case 1, coarse meshes with splitting; Case 2, uniformly refined meshes with splitting; and Case 3, fine meshes with splitting. **a** Cartesian representation shows the average E_{length} over 10 meshes for each angle with band representing the standard deviation, and **b** histogram representation

Contrary to the investigation of E_{length}, the level of refinement is the controlling factor when considering the error in the Hausdorff distance, $E_{\text{Hausdorff}}$. As the mesh is refined, the Hausdorff distance decreases, as evident in Fig. 11. We see that the uniformly refined meshes result in an $E_{\text{Hausdorff}}$ that is very similar to that of the fine meshes. Since the proposed refinement scheme is applied adaptively (i.e. when and where it is needed) in our dynamic fracture simulations we gain the benefit of a smaller Hausdorff distance without needing to refine the entire domain.

Next, we repeat the previous geometric studies on the same sets of meshes; however, this time, we add the element splitting capability proposed by

Leon et al. (2014), and summarized in Sect. 2.2. The results are similarly presented in two graphical representations, in Figs. 12 and 13. The scales in Figs. 12 and 13 match those of Figs. 10 and 11, respectively.

As illustrated in Fig. 12, the error for all three mesh types drops significantly when elements are allowed to be split; which is in agreement with the findings of Leon et al. (2014). However, even in the presence of element splitting, mesh refinement only slightly reduces the error in the crack length for polygonal meshes. The uniformly refined meshes with element splitting show the lowest error with the smallest standard deviations of all the cases considered in this work, and supports our motivation for using this refinement scheme.
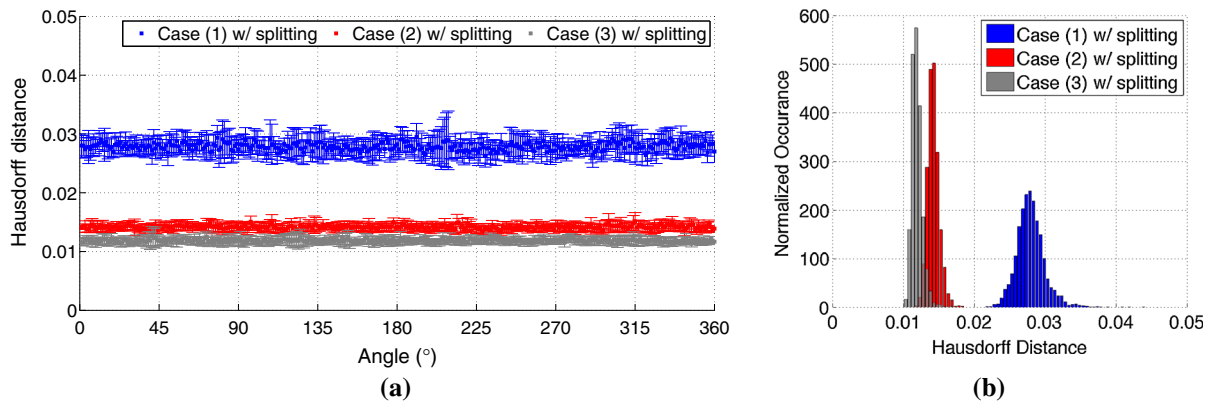
Fig. 13 Hausdorff distances, $E_{\text{Hausdorff}}$ for Case 1, coarse meshes with splitting; Case 2, uniformly refined meshes with splitting; and Case 3, fine meshes with splitting. **a** Cartesian representation shows the average $E_{\text{Hausdorff}}$ over 10 meshes for each angle with band representing the standard deviation, and **b** histogram representation

Finally, we see a slight improvement in the average Hausdorff distance when element splitting is introduced. Mainly, the range of the Hausdorff distances becomes smaller for all mesh types considered, as illustrated in Fig. 13b. Similar to the results without splitting, the uniformly refined meshes have nearly as low a Hausdorff distance as the fine meshes.

These studies demonstrate that the adaptive refinement scheme with on-the-fly element splitting is the best suited, of the six cases examined, for dynamic fracture simulations. The ability of the mesh to represent a straight line is better than any other case. Moreover, the error in deviation from a straight line is nearly the same as the error for a fine meshes; however, the computational storage will be much lower because the adaptivity is done on an as-needed basis. This additional advantage will be explored in the examples in Sect. 5.

4 Constitutive relations

One of the primary critiques of the cohesive element approach to modeling fracture is its inherent mesh dependency, due to the limitation that fracture can only propagate along element edges. While we have shown in Sect. 3 that this mesh dependency is minimal when we use the geometrically and topologically unstructured methods outlined in this paper, we also investigate the use of materially unstructured means to reducing mesh dependency Zhou and Molinari (2004). A feature of the cohesive element method is the ability to separate the constitutive relation of the bulk material from that of the cohesive model. In this section we discuss the bulk and cohesive models used in this investigation, and the means by which we investigate microscale heterogeneities.

4.1 Bulk material model

The focus of this paper is on either homogeneous or homogenized materials; however, in reality, it is recognized that all materials have inherent inhomogeneities at the microscale. To account for these microscale inhomogeneities, the primary properties of the material are randomly assigned. The bulk material is elastic with an assigned elastic modulus, E, and Poisson's ratio, ν. While the elastic modulus is a global parameter, the modulus at the microscale is varied. To model this variation numerically, the elastic modulus is assigned to follow a statistically random Weibull (1939) distribution:

$$E = E_o(-\ln(1 - \rho)^{1/m}) \tag{12}$$

where E_o is the average elastic modulus, ρ is a randomly generated number between 0 and 1, and m is the Weibull modulus.

4.2 Cohesive model

Extrinsic cohesive elements are adaptively inserted into the mesh as the simulation progresses, as illustrated

Fig. 14 Traction separation relations for **a** normal direction ($\phi_n = 100$ N/m, $\sigma_{max} = 40$ MPa, $\alpha = 3.0$, and $\lambda_n = 0.1$), **b** tangential direction ($\phi_t = 200$ N/m, $\sigma_{max} = 30$ MPa, $\beta = 2.0$, and $\lambda_t = 0.2$)

(a)

(b)
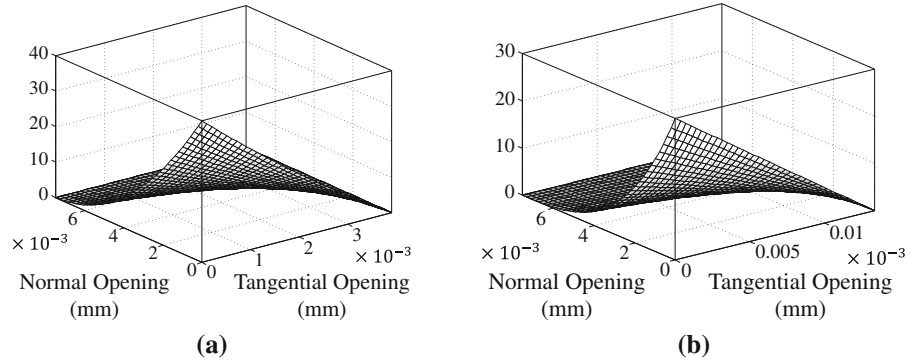
in Fig. 7. In order to adaptively insert extrinsic cohesive elements and consistently modify the topology of the mesh, a topological data structure; which is able to efficiently retrieve and update adjacency relations, is required. This study uses the topological data structure TopS (Celes et al. 2005a, b) to efficiently store, retrieve and update the pertinent adjacency relations. By design, TopS explicitly stores the vertex and edge information, and the element-to-element adjacency relations. Within this framework, the insertion of cohesive elements and the retrieval of adjacency information occurs in linear time (Paulino et al. 2008).

The constitutive relation chosen for the cohesive elements in this study is the potential-based Park–Paulino–Roesler (PPR) cohesive model, however, other constitutive relations can also be employed (Klein et al. 2000). The details of the model have been well documented, and may be found in the principal publication (Park et al. 2009). Briefly, the extrinsic PPR cohesive relation is polynomial-based with six user-defined inputs: cohesive fracture energies (ϕ_n, ϕ_t); cohesive strengths (σ_n, τ_t); and cohesive shape parameters (α, β). The six user inputs allow for an adaptable model that is able to capture a variety of physical responses. The tractions are derived by taking the derivatives of a potential, Ψ, with respect to the crack opening widths (Δ_n, Δ_t) and are explicitly expressed as:

$$T_n\left(\Delta_n, \Delta_t\right) = \frac{\partial \Psi}{\partial \Delta_n} = -\alpha \frac{\Gamma_n}{\delta_n}\left(1 - \frac{\Delta_n}{\delta_n}\right)^{\alpha-1}$$
$$\times \left[\Gamma_t\left(1 - \frac{|\Delta_t|}{\delta_t}\right)^{\beta} + \langle \phi_t - \phi_n \rangle\right],$$
(13)

$$T_t\left(\Delta_n, \Delta_t\right) = \frac{\partial \Psi}{\partial \Delta_t} = -\beta \frac{\Gamma_t}{\delta_t}\left(1 - \frac{|\Delta_t|}{\delta_t}\right)^{\beta-1}$$
$$\times \left[\Gamma_n\left(1 - \frac{\Delta_n}{\delta_n}\right)^{\alpha} + \langle \phi_n - \phi_t \rangle\right]\frac{\Delta_t}{|\Delta_t|}.$$
(14)

where Δ_n and Δ_t are the crack opening widths in the normal and tangential directions, respectively; and Γ_n and Γ_t are energy constants in the normal and tangential directions, respectively. Sample extrinsic traction–separation relations are illustrated in Fig. 14.

In order to further investigate the influence of materially unstructured means on reducing mesh dependency, we also vary the primary cohesive parameters. Both the cohesive strength and fracture energy, attributes of the cohesive elements, are individually selected to follow a modified weakest link Weibull distribution, where the probability of a cohesive element having a lower cohesive strength or fracture energy increases with increasing element size Zhou and Molinari (2004):

$$\gamma = \frac{L_s^{1/m}}{L_f^{1/m}}\gamma_o(-\ln(1-\rho)^{1/m})$$
(15)

where γ_o is the average cohesive property (in this paper, γ_o is either the cohesive strength or the cohesive fracture energy), L_f is the length of the cohesive element, L_s is a scaling parameter, and m is the Weibull modulus. For a uniform mesh, the scaling parameter is selected to be the average facet length; whereas, for an adaptively refined mesh, the scaling parameter is selected to be the average facet length of an equivalent uniformly refined mesh. Figure 15 illustrates the distribution of facet lengths for a typical mesh with approximately 16,000 facets before refinement, and approximately 67,000 facets after refinement. This approach was proposed by Zhou and Molinari (2004) as a means
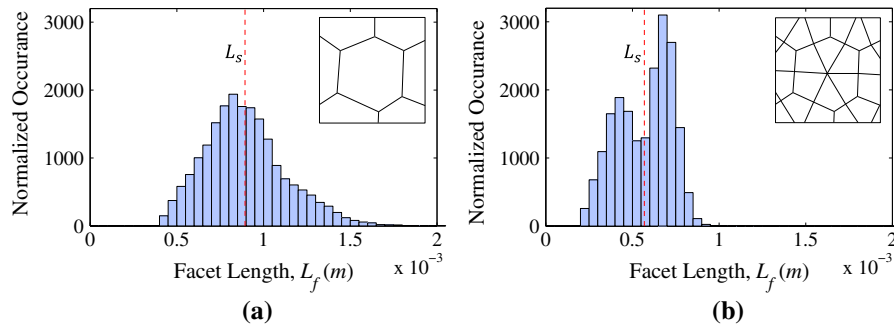
Fig. 15 Facet length distribution for a typical random mesh consisting of 6,000 elements. There are approximately 16,000 facets before refinement and approximately 67,000 facets after uniform refinement. The domain for this example is 100 mm × 100 mm.

a Uniform discretization, and **b** uniformly refined discretization. The dashed line corresponds to the average facet length in the mesh (L_s), and is equivalent for both the uniformly refined mesh and the adaptively refined mesh
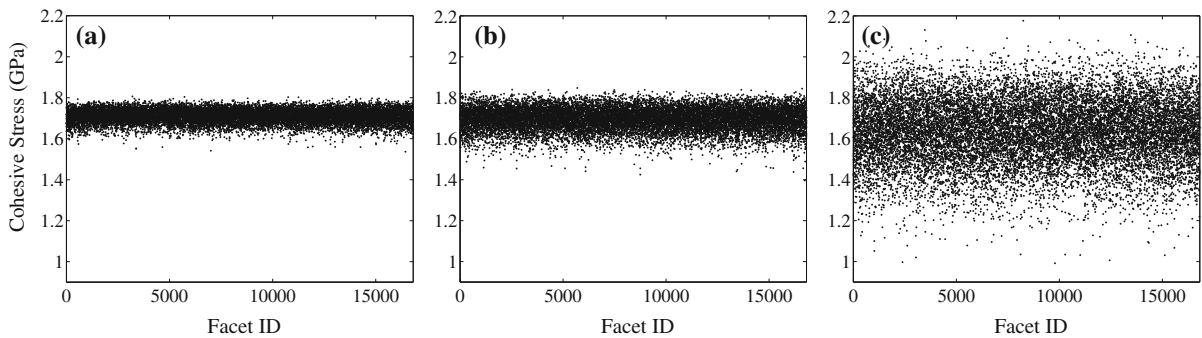

Fig. 16 Example statistical distribution for a Weibull Modulus of **a** $m = 50$, **b** $m = 30$ and **c** $m = 10$

to address mesh dependency from a material perspective. While it has proven useful in many situations with triangular and tetrahedral elements, it has not been investigated with polygonal elements.

To illustrate the effect of the Weibull modulus on the material distribution, a sample mesh with 16,000 randomly numbered facets was generated, and cohesive properties were randomly assigned to the facets. For example, when a mesh with an average cohesive strength, $\sigma_o = 1.733$ GPa, was modeled, the resulting variation of cohesive strength for $m = 50, 30$, and 10 is illustrated in Fig. 16. Clearly, the smaller the value of m, the greater the range of assigned properties and thus the greater the overall heterogeneity in the material.

5 Example problems

In this section, three numerical example problems are presented. The first example considers the impact of a

double notched test specimen; which has well known fracture behavior. This will serve as the benchmark for our analysis, and we will use this opportunity to investigate the effect that the radius of the zone of refinement has on the fracture behavior. The second example focuses on the mixed-mode fracture behavior of a notched plate with a hole under impact load. The third example considers microbranching behavior. All the examples have related experimental results in the literature. In order to compare the various schemes highlighted in this paper, five cases are analyzed: (1) a coarse polygonal mesh, (2) a coarse polygonal mesh with element splitting, (3) an adaptively refined coarse polygonal mesh with element splitting, (4) a fine polygonal mesh, and (5) a fine quadrilateral mesh with element splitting. The five schemes are illustrated in Fig. 17. The fine quadrilateral mesh is geometrically equivalent to the coarse polygonal mesh, where each polygon is refined with the scheme illustrated in Fig. 5.
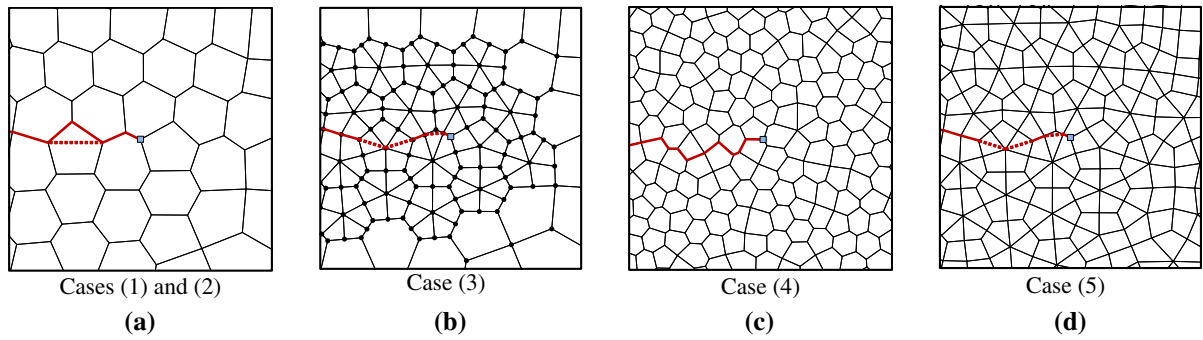
Cases (1) and (2)   Case (3)   Case (4)   Case (5)
(a)   **(b)**   **(c)**   **(d)**

Fig. 17 The five discretization schemes considered in this investigation: **a** a coarse polygonal mesh with and without element splitting, **b** an adaptively refined coarse polygonal mesh with element splitting (nodes are depicted to illustrate the ability of the polygonal elements to adaptively account for hanging nodes),

c a fine polygonal mesh, and **d** a fine quadrilateral mesh with element splitting. Note that the element splitting isn't explicitly represented in the mesh, as it occurs on-the-fly; which is why *dashed lines* are used to depict split elements
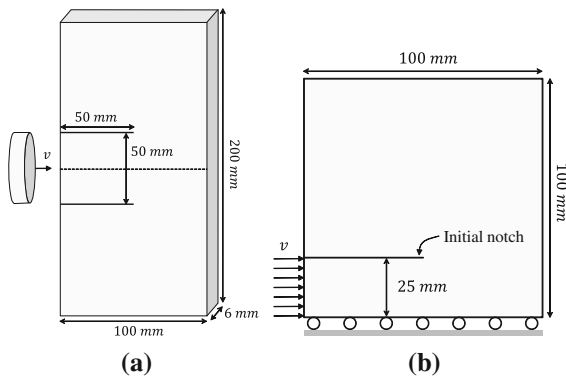

(a)   **(b)**

Fig. 18 a The doubled notched plate test specimen used by Kalthoff and Winkler Kalthoff and Winkler (1987), and **b** symmetric model used for computations

5.1 Double notched plate specimen

Kalthoff and Winkler (1987) studied the crack propagation of a double-notched plate specimen under impact load, as illustrated in Fig. 18a. They show that, for this specimen, the failure mechanism changes from brittle to ductile failure as the impact velocity increases. In the case of brittle failure (low rates of loading), cracking initiates at an angle of approximately 70° from the initial plane of the notch. At higher rates of loading, the failure mechanism is dominated by plastic shear, and the crack initiates at an angle of approximately −10°. In this example we focus on the case of brittle fracture, and attempt to capture the initiation angle of 70°.

Numerically, this problem has been investigated by many researchers. Belytschko et al. Belytschko et al.

(2003) used discontinuous enrichment functions, in the extended finite element method, and captured a crack initiation angle of 58° with an average crack tip velocity of about 75 % the Rayleigh wave speed. Zhang and Paulino (2005) used intrinsic cohesive elements, inserted into the mesh a priori, and found a crack initiation angle of between 72° and 74°, with an average crack tip velocity of about 65 % the Rayleigh wave speed. Most recently, Park et al. (2012) used extrinsic cohesive elements with adaptive refinement and coarsening on a 4k mesh. They capture a crack initiation angle of approximately 62°, with an average crack tip velocity of 71 % the Rayleigh wave speed.

Due to the symmetry of the problem, the geometry can be reduced to that illustrated in Fig. 18b. The impact velocity is 16.54 m/s, and is linearly ramped up over 1 μs. Maraging steel, designated as 18Ni(300), as per the American National Standards Institute, is used as the representative material. The elastic modulus of the steel is 190 GPa, the Poisson's ratio is 0.3, the density is 8,000 kg/m³, and the plane strain assumption is employed. The mode I and mode II fracture parameters are assumed to be equivalent, with a fracture energy of 22.2 kJ/m², a cohesive strength of 1.733 GPa, and a shape parameter of 2.

In order to determine the effect that the chosen radius of refinement has on the fracture pattern during adaptively refined simulations, we model this problem with a variety of selected radii. Cases with a radius of $r = 2$, 4, and 6 mm are considered, with a starting mesh of 6,000 polygonal elements. The smallest radius we consider ($r = 2$ mm) is a result of the mesh size;
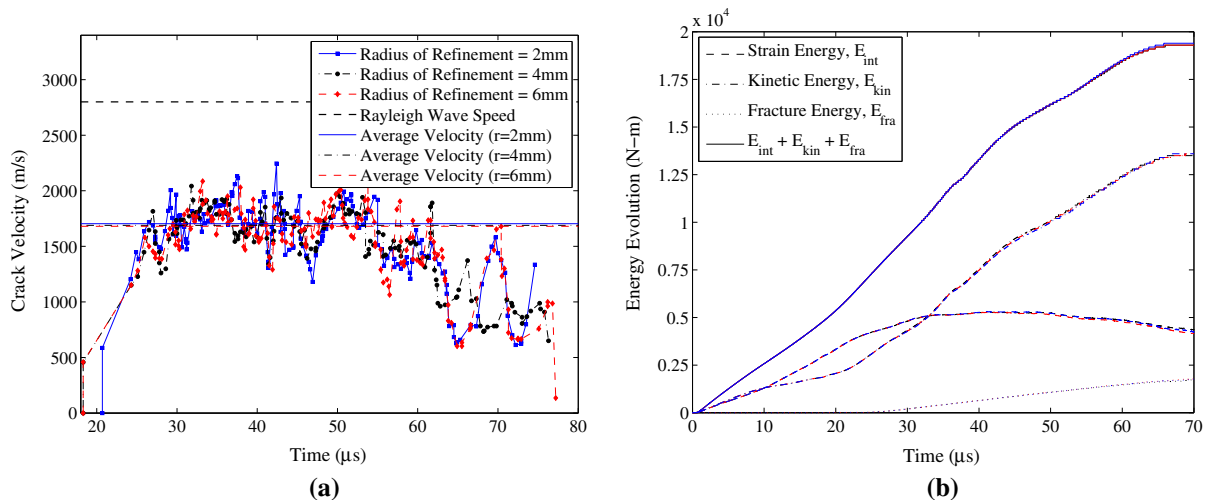
Fig. 19 a Velocity of crack tip, and **b** evolution of energy for the various values of the radius of refinement. The average velocity is calculated between a time of 25 and 50 μs

with this radius there are approximately 10 polygonal elements refined around each crack tip. When a radius of $r = 1$ mm is selected only two elements are refined, resulting in the presence of unrefined elements at the crack tip. The size of the starting mesh was determined through a mesh refinement study and shown to display sufficiently accurate results. The velocity of the crack tip, and the evolution of energy are the two parameters of interest in this investigation. For the purposes of computing the crack tip velocity, the crack tip is defined as the individual crack tip which is the greatest distance from the end of the initial notch. The velocity of the crack tip, illustrated in Fig. 19a, displays similar trends for each radius of refinement. For the case of $r = 2$ mm, the crack initiates at a later time then in the other cases; however, the average velocity for each case is similar (approximately 60 % of the Rayleigh wave speed), as illustrated in Fig. 19a.

When we consider the evolution of energy, the results again indicate that the radius of refinement has only a minor effect. The evolution of energy for each case, illustrated in Fig. 19b, is comprised of the strain (E_{int}), kinetic (E_{kin}) and fracture (E_{fra}) energies. The fracture energy is zero up to the point of crack initiation, then steadily increases over time. The strain energy increases due to the impact, but decreases over time as the crack propagates. The external energy is equal to the sum of the strain, kinetic, and impact energies. The sum of the energies is similar for all cases; however, a small discrepancy in the strain energy is

observed beyond approximately 60 μs. Based on these results, and due to the small variation in computational cost between the three refinement radii, we select a radius of $r = 4$ mm for all cases we consider.

The base, coarse polygonal mesh, contains 6,000 elements. When uniformly refined with quadrilateral elements, the mesh has 33,254 elements; which is the number of elements used to discretize the fine polygonal mesh. When adaptive refinement is used, a zone with a 4 mm radius is initially refined at the notch tip, as illustrated in Fig. 20a. For this case, the refined finite element mesh discretizations at 47.5 and 77.5 μs are illustrated in Fig. 20c, e, respectively. Beside each mesh in Fig. 20 we provide the composition of the mesh, which illustrates the evolution of the 4-gons throughout the simulation.

For all cases, the global fracture angles are similar (68°–72°), and are in good agreement with the experimentally observed angle of 70°. However, the fracture surfaces for the coarse and fine polygonal meshes are noticeably biased by the polygonal element shapes, as illustrated by the fluctuating crack patterns in Fig. 21a. Both coarse polygonal meshes (with and without splitting) display poor agreement with the expected fracture initiation angle, and produce the highest global fracture angles.

Even though the coarse polygonal meshes produce fracture surfaces that are biased by the shape of the elements, the crack velocity for each case displays similar trends. The crack initiates approximately 20 μs

n	n-gon	number of n-gons
3	△	1
4	□	450
5	⬠	2361
6	⬡	3159
7	⬠	179
($8 \leq n \leq 11$)		7
Total Elements		6157

(a) **(b)**

n	n-gon	number of n-gons
3	△	143
4	□	1602
5	⬠	2295
6	⬡	2968
7	⬠	190
($8 \leq n \leq 11$)		43
Total Elements		7241

(c) **(d)**

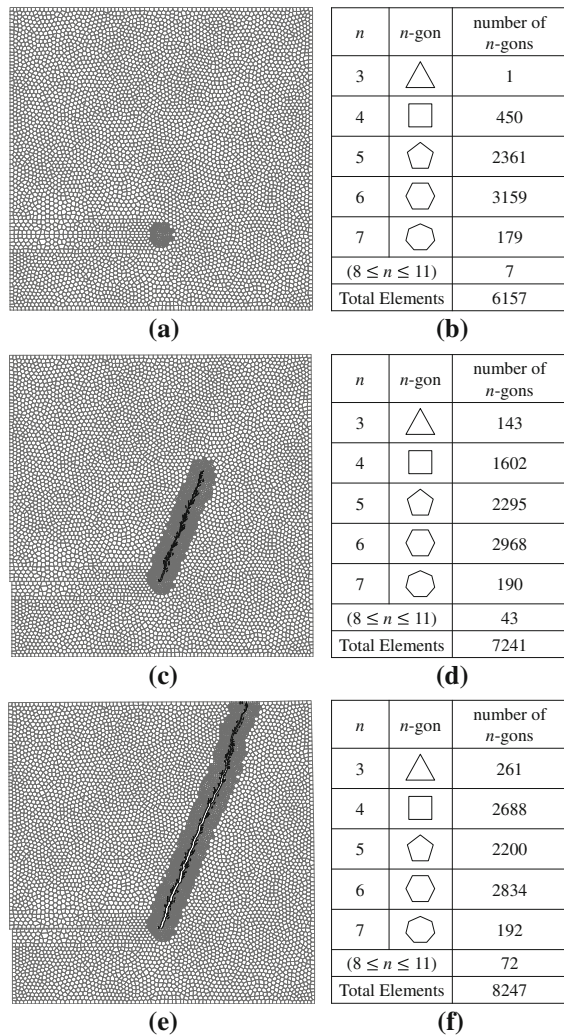| n	n-gon	number of n-gons
3	△	261
4	□	2688
5	⬠	2200
6	⬡	2834
7	⬠	192
($8 \leq n \leq 11$)		72
Total Elements		8247

(e) **(f)**

Fig. 20 For the case of adaptive refinement with element splitting: **a** initial mesh discretization, with zone of refinement at notch tip, **b** the composition of the initial mesh, **c** intermediate mesh at 47.5 μs, **d** the composition of the intermediate mesh, **e** final mesh at 82.5 μs, and **f** the composition of the final mesh

after impact, steeply ramps up, and fluctuates greatly thereafter, as illustrated in Fig. 21b. After roughly 50μs the velocity begins to gradually decrease. In all cases the average velocity is approximately 1,675 m/s (or approximately 60 % of the Rayleigh wave speed). These results correspond well with those published in the literature (Zhang and Paulino 2005; Park et al. 2012).

The computational time is listed in Table 1. We compare the time it takes for the specimen to fracture completely, as the number of iterations for each mesh to fracture varies, due to the variations in path length and

corresponding element type. The total cost is lowest for a coarse polygonal mesh with element splitting, and highest for the fine polygonal mesh. Alternatively, one could make comparisons based on the cost per iteration. In this case, the coarse polygonal mesh becomes the lowest cost option, and has a smaller cost per iteration than the adaptively refined case. This result is in line with expectations, as the adaptively refined mesh; while it starts with the same discretization, adds elements (and nodes) to the problem as the simulation progresses. Also notable is that computations using the adaptive refinement scheme, when compared to those for the uniformly refined mesh of the same effective discretization, are approximately 3.4 times faster.

5.2 Notched plate with hole

This example highlights the mixed-mode fracture of a notched PMMA plate with a hole. This problem was investigated experimentally by Grégoire et al. (2007) using the geometry illustrated in Fig. 22a. The experiments demonstrate a fracture initiation angle of approximately 37.5°. The crack initially propagates in a mixed-mode manner then transitions into a mode I crack a short while after initiation. Numerically, this problem has been investigated using the XFEM method by Grégoire et al. (2007) and Gravouil et al. (2009); and using the polygonal scaled boundary finite element method by Ooi et al. (2012b, 2013). To the best of the authors knowledge, this problem has not been investigated using the cohesive element approach.

Experimentally, the specimen is impacted using a Hopkinson bar (Hopkinson 1914) with a diameter of 40 mm. Numerically, the impact is described by an applied velocity that ramps up to 8 m/s over a period of 100 μs then ramps down to 7 m/s over a period of 600 μs, as illustrated in Fig. 22b. The mesh contains 6,000 elements and a radius of refinement of 4 mm is used. The PMMA has an average elastic modulus of 3.3 GPa, a Poisson's ratio of 0.42, a density of 1,180 kg/m^3, and the plane strain condition is employed. The average mode I fracture energy (ϕ_n), cohesive strength (σ_n), and shape parameter (α) are set as 352.4 N/m, 62.1 MPa and 2, respectively. The mode II fracture properties are assumed to be the same as the mode I fracture properties, and the influence of the distribution of material properties on the global fracture pattern is investigated.
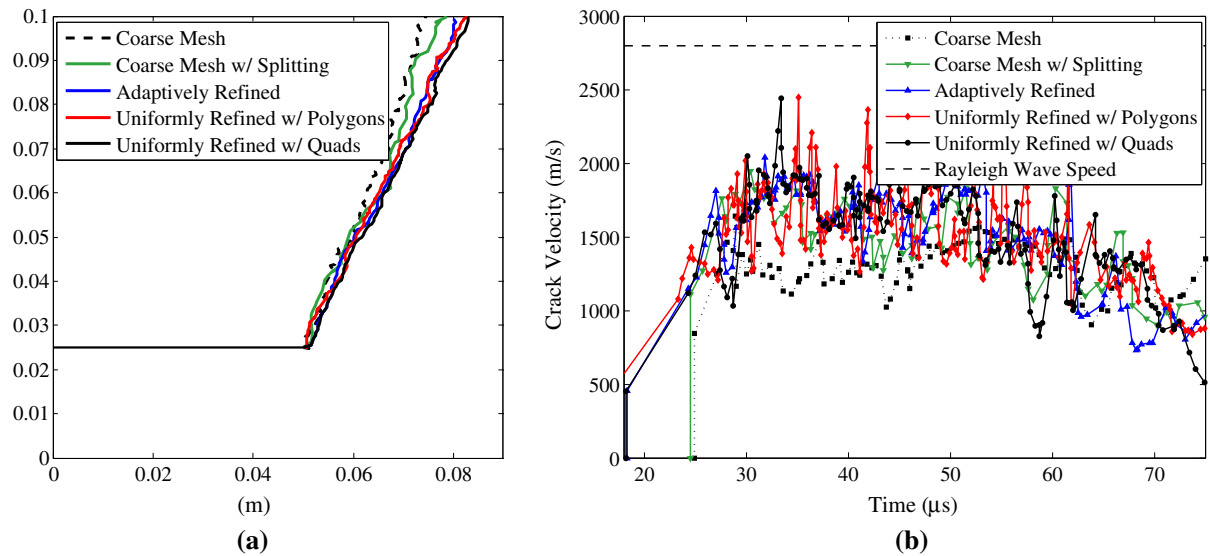
Fig. 21 Comparison of **a** the crack paths, and **b** the crack tip velocity for the five cases considered

Table 1 Summary of computational cost to simulate the various cases considered for the double notched plate example

Case	Elements	Nodes	Cost (min)	Iterations to fracture	Cost/iteration (ms)
1	6,000	10,815	25.7	18,250	84.5
2	6,000	10,815	24.3	16,900	86.3
3	**6,000**	**10,815**	**25.3**	**16,500**	**92.0**
4	33,254	60,314	154.2	16,400	564.1
5	33,254	33,629	85.5	16,400	312.8

The five cases correspond to: (1) a coarse polygonal mesh, (2) a coarse polygonal mesh with element splitting, (3) an adaptively refined coarse polygonal mesh with element splitting (the final mesh contains 8,247 elements and 12,994 nodes), (4) a fine polygonal mesh, and (5) a fine quadrilateral mesh with element splitting. The elements and nodes correspond to the initial discretization (the base mesh), and the wall-clock time is recorded in minutes. The time step was held constant at $\Delta t = 5 \times 10^{-9}\,\mu$s. The bold values correspond to the newly proposed adaptive refinement scheme
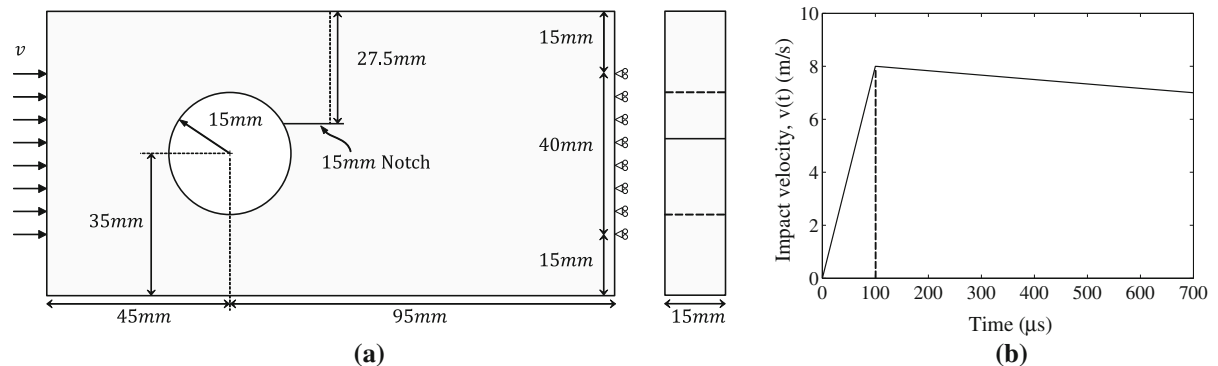

Fig. 22 **a** Geometry of the notched plate with hole, and **b** impact velocity
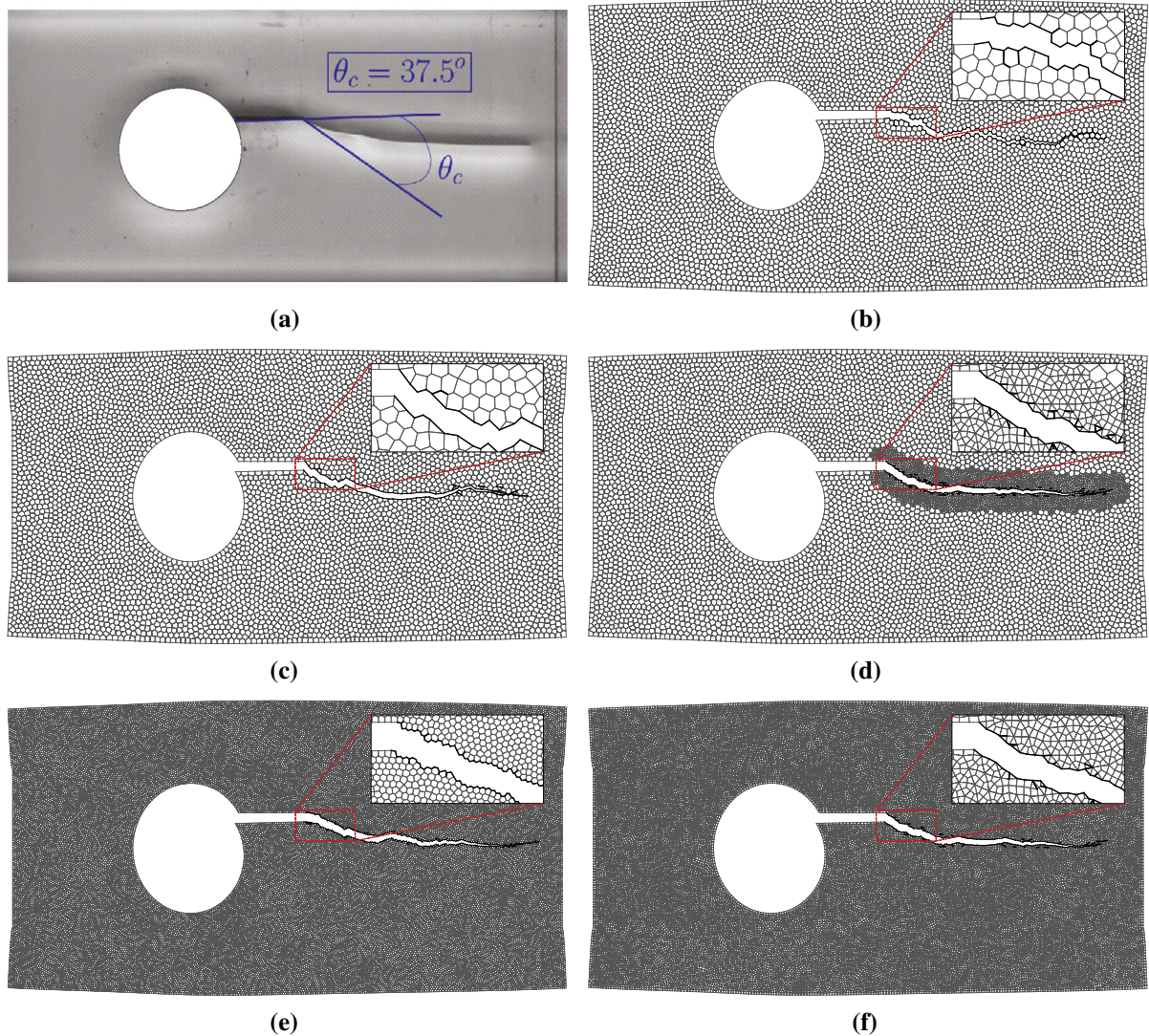
Fig. 23 Results from the notched plate with hole study. **a** Experimentally obtained fracture pattern and crack initiation angle of approximately 37.5° (Figure extracted from Grégoire et al. 2007). Simulated results for **b** a coarse polygonal mesh, **c** a coarse polygonal mesh with element splitting, **d** an adaptively refined coarse polygonal mesh with element splitting, **e** a fine polygonal mesh, and **f** a fine quadrilateral mesh with element splitting

The experimentally obtained fracture pattern and crack initiation angle is illustrated in Fig. 23a. Sample results from our simulations are presented in Fig. 23. In Fig. 23b the coarse polygonal mesh displays a crack initiation angle of approximately 16°. This is not significantly improved when a fine polygonal mesh is used, as the crack in this case initiates at an angle of approximately 22° (Fig. 23e). *When elements are allowed to be split* (Fig. 23c), *the crack initiation angle increases to approximately* 31°, *helping support our argument that element splitting is a signifi-*

cant step towards obtaining accurate fracture patterns with polygonal elements. However, these results still do not approach the experimentally observed crack initiation angle of 37.5°, and do not quite transition to the mode I cracks we expect. Alternatively, when we use an adaptively refined mesh (Fig. 23d) or an a equivalent uniformly refined with quadrilateral elements (Fig. 23f), we observe a much smoother fracture surface, with the crack initiating at an angle of approximately 35° and transitioning from a mixed-mode crack to a mode I crack a short while after initiation—
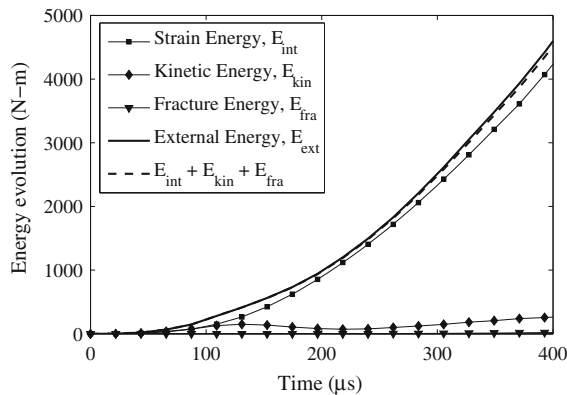
Fig. 24 Evolution of energy for the notched plate with hole using adaptive refinement with splitting

results which approach those observed experimentally.

An investigation of energy evolution is conducted for the case of adaptive refinement, as illustrated in Fig. 24. The sum of the strain energy, kinetic energy and fracture energy shows good agreement with the external energy imparted on the specimen by the Hopkinson bar. The fracture energy remains equal to zero up until the point of crack initiation, and increases over time, however, it does not contribute significantly to the overall energy. The computational time is compared in Table 2 for the five cases considered (see Fig. 17). The time step was set at $\Delta t = 2 \times 10^{-8}\,\mu\text{s}$, based on the Courant–Friedrichs–Lewy stability condition (Bathe 1996), and the number of iterations to fracture was 22,500 for all cases. The coarse polygonal mesh has the lowest cost per iteration, and when adaptive operators are included (splitting and adaptive refinement), the cost increases slightly. In comparison to the equiva-

lent result obtained using a uniformly refined mesh with quadrilateral elements, the adaptive refinement scheme is more than four times faster.

In order to investigate the effect that microstructural heterogeneities might have on the global fracture patterns, we varied the bulk elastic modulus, the cohesive fracture energy and the cohesive strength as discussed in Sect. 4. The study was conducted on the first three cases in this paper; a coarse polygonal mesh, a coarse polygonal mesh with element splitting and the adaptively refined coarse polygonal mesh, see Fig. 17. For each material property considered, three different Weibull moduli were selected, $m = 10, 30$, and 50, and for each Weibull modulus three different random instances were simulated. Based on the study, statistically distributing the material properties has a negligible effect on the global fracture patterns. For sake of brevity, not all of the results are shown here, but typical results are illustrated in Fig. 25. We illustrate the two meshes in most need of improvement, coarse polygonal meshes with and without element splitting, with the widest variation of material properties ($m = 10$) for each of the properties considered. From the results, it is clear that using a statistical distribution of material properties to overcome mesh dependency does not improve the global fracture patterns for the geometrically restrictive polygonal meshes.

5.3 Microbranching

The microbranching instability in brittle materials undergoing dynamic fracture was experimentally investigated by Sharon et al. (1995) and Sharon and Fineberg

Table 2 Summary of computational cost to simulate the various cases considered for the notched plate with hole example

Case	Elements	Nodes	Cost (min)	Cost/iteration (ms)	Crack initiation angle (°)
1	6,000	11,460	29.5	78.7	16
2	6,000	11,460	30.4	81.1	31
3	**6,000**	**11,460**	**32.8**	**87.5**	**35**
4	34,503	68,195	190.3	507.5	22
5	34,503	34,902	135.0	360.0	35

The five cases correspond to: (1) a coarse polygonal mesh, (2) a coarse polygonal mesh with element splitting, (3) an adaptively refined coarse polygonal mesh with element splitting (the final mesh contains 7,873 elements and 13,193 nodes), (4) a fine polygonal mesh, and (5) a fine quadrilateral mesh with element splitting. The elements and nodes correspond to the initial discretization (the base mesh), and the wall-clock time is recorded in minutes. The time step was held constant at $\Delta t = 2 \times 10^{-8}\,\mu\text{s}$. The bold values correspond to the newly proposed adaptive refinement scheme
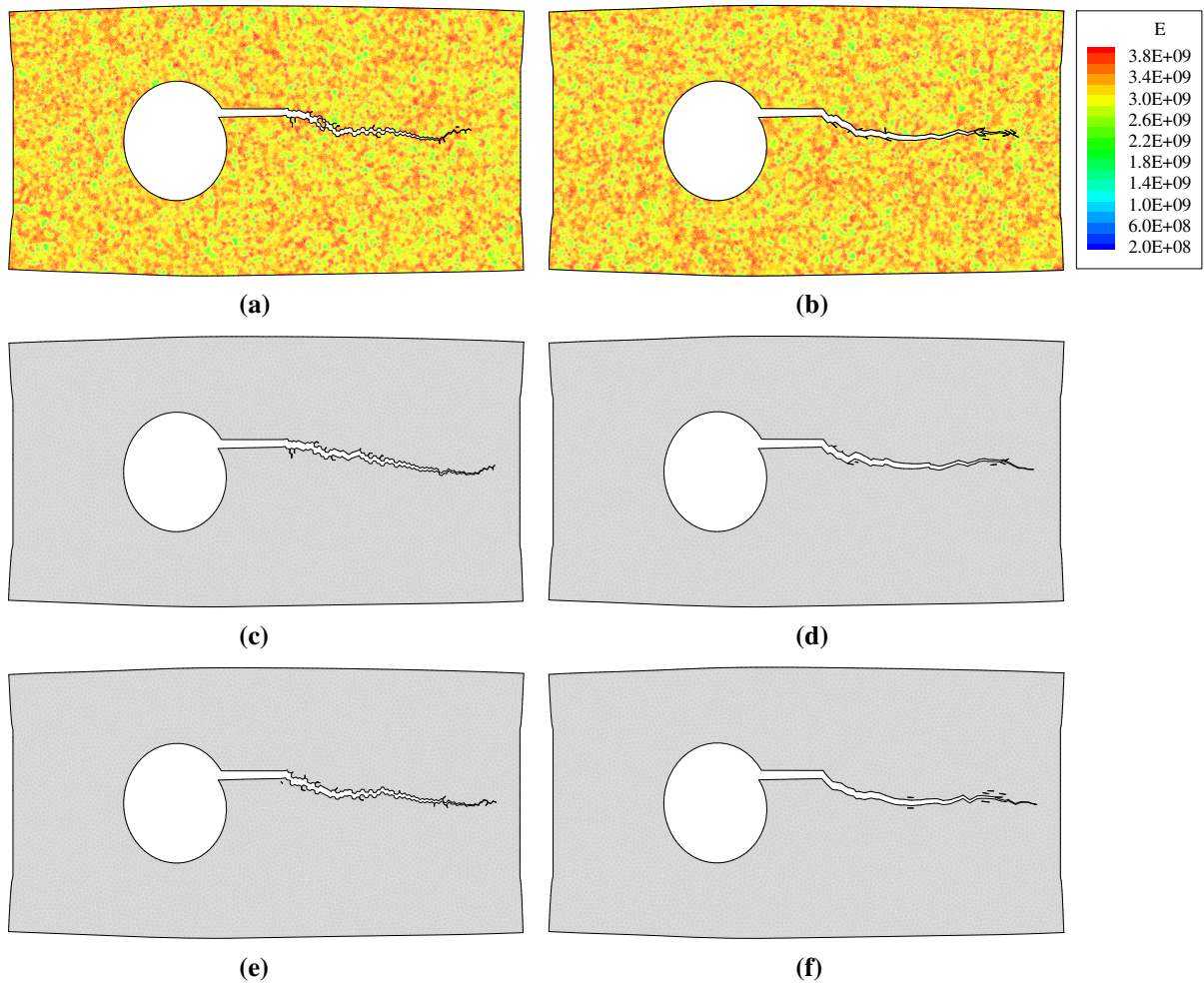
Fig. 25 Global fracture patterns for the notched plate with hole problem when the material is statistically distributed. Results are for: **a**, **b** a variation in elastic modulus for the case of a coarse polygonal mesh without element splitting and with element splitting, respectively; **c**, **d** a variation in cohesive energy (140 N/m $\leq \phi_n \leq$ 440 N/m) for the same cases, respectively; and **e**, **f** a variation in cohesive strength (25 MPa $\leq \sigma_n \leq$ 78 MPa) for the same cases, respectively. Results are shown for a Weibull modulus of $m = 10$, but illustrate the minor effect that the materially unstructured method has on global fracture patterns when using unstructured polygonal elements

(1996). They conducted experiments on PMMA sheets with a width of 50–200 mm and a length of 200–400 mm. Among others, Zhang et al. (2007) illustrated that equivalent behavior can be achieved numerically, at a lower cost, with a reduced dimension model. Thus, the numerical study is conducted on a reduced dimension model having a width of 4 mm, and a length of 16 mm, as illustrated in Fig. 26 (Zhang et al. 2007). The PMMA sheet has an average elastic modulus of 3.24 GPa, a Poisson's ratio of 0.35, a density of 1,190 kg/m^3, and the plane stress condition is employed. The average mode I fracture energy (ϕ_n), cohesive strength (σ_n), and shape parameter (α) are set as 352.4 N/m, 129.6 MPa

and 2, respectively. The mode II fracture properties are assumed to be the same as the mode I fracture properties, and the influence of the distribution of cohesive material properties on the global fracture pattern and crack tip velocity is investigated.

A number of researchers have investigated this problem numerically. For instances Miller et al. (1999) used intrinsic cohesive elements, dispersed throughout the model, to investigate the energy dissipation due to microbranching. They show that crack branching leads to energy dissipation as the crack velocity increases; which is consistent with the assertion made by Sharon et al. 1995 and Sharon and Fineberg
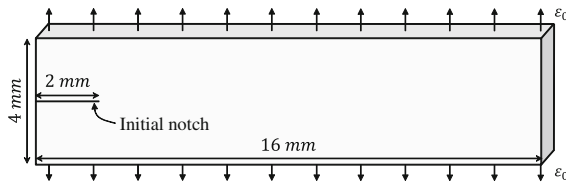
Fig. 26 Geometry and boundary conditions used to investigate the microbranching instability in a PMMA sheet. A strain of $\epsilon_0 = 0.015$ is applied to the upper and lower surface of the specimen

(1996) based on their experimental results. Zhang et al. (2007) used extrinsic cohesive elements, within a topological data structure, to capture the microbranching instability. Their simulations are conducted on a structured 4k mesh; which leads to similar angles of initiation for the microbranches, and capture behavior in good agreement with experiments. Most recently, Paulino et al. (2010) used nodal perturbation and edge-swap operators to make a structured 4k mesh unstructured. Their results indicate that unstructured meshes capture varied microbranching angles; and lead to results which are more consistent with experiments.

For this investigation, we consider the same five cases as before (Fig. 17): (1) a coarse polygonal mesh, (2) a coarse polygonal mesh with element splitting, (3) an adaptively refined coarse polygonal mesh (4) a fine polygonal mesh, and (5) a fine quadrilateral mesh. The base, coarse polygonal mesh, contains 4,000 elements. When uniformly refined with quadrilateral elements, the mesh has 22,039 elements; which is the number of elements used to discretize the fine polygonal mesh. For the cases with adaptive refinement, a zone with a 0.4 mm radius is refined at each crack tip. The results of the investigation are illustrated in Fig. 27. The case for the coarse polygonal mesh (Fig. 27a) results in a fracture surface biased by the polygonal element shapes, and little crack branching. When adaptively refined with quadrilateral elements (Fig. 27c), the fracture surface is smoother, and the frequency of micro and macro branching increases. When uniformly refined with quadrilateral elements (Fig. 27e), we get similar behavior to that for the case of adaptive refinement. For the adaptively refined case, and the two fine cases, the fracture patterns agree well with both previous numerical investigations and experimental results.

The horizontal velocity of the crack tip is tracked, for each case, and plotted in Fig. 28a. For the purposes of computing the crack tip velocity, the crack tip is defined as the individual crack tip which is the greatest horizontal distance from the end of the initial notch. The average velocity of each case is also plotted, and is in close agreement with one another. Since the crack tip
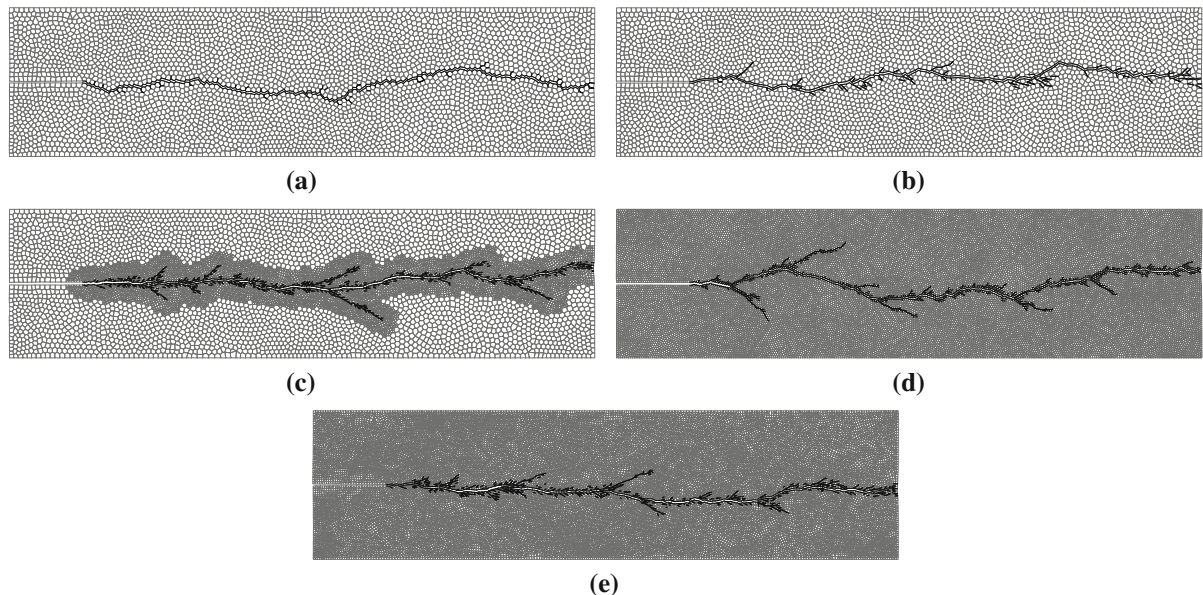

Fig. 27 Simulated results for **a** a coarse polygonal mesh **b** a coarse polygonal mesh with element splitting, **c** an adaptively refined coarse polygonal mesh, **d** a fine polygonal mesh, and **e** a fine quadrilateral mesh with element splitting
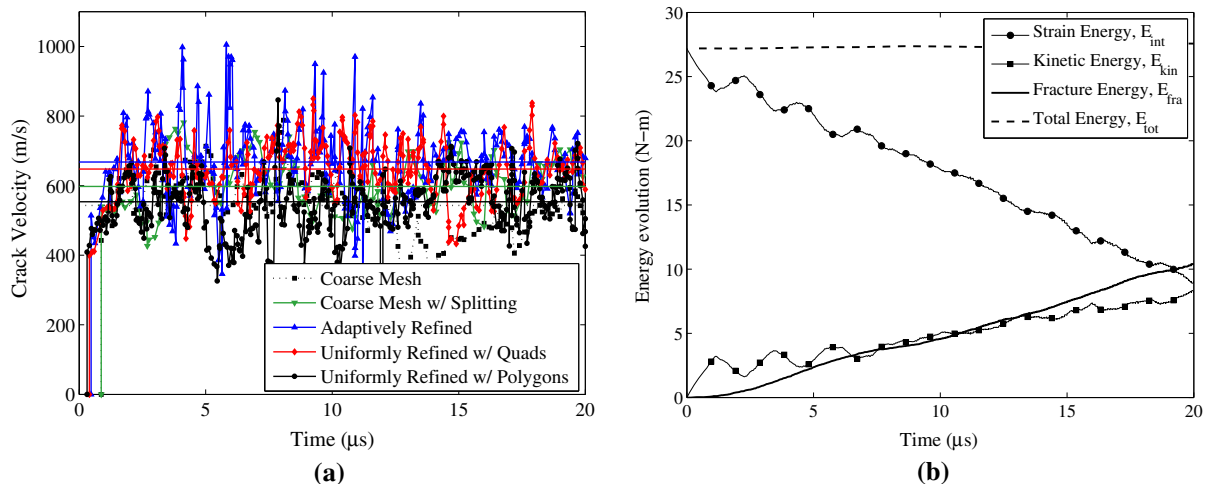
Fig. 28 **a** Velocity of crack tip for the five cases considered. The average velocities are included as *horizontal lines*. **b** Evolution of energy for the microbranching specimen using adaptive refinement with splitting

velocity fluctuates significantly while the crack propagates, the average velocity is only representative of the overall trend and should not be taken as a precise value. The average velocity is lowest for the case of a coarse polygonal mesh (approximately 543 m/s), and is highest for the adaptively refined case (approximately 667 m/s). All cases have crack tip velocities that fall within the range of those determined experimentally (as illustrated in Figure 4 in Sharon and Fineberg 1996).

Similarly to the previous examples, the evolution of energy is computed for the case of adaptive refinement and illustrated in Fig. 28b. Because there is no external work in this problem ($E_{ext} = 0$), the total energy (E_{tot}) is the sum of the strain energy (E_{int}), the kinetic energy (E_{kin}), and the fracture energy (E_{fra}). The total energy remains constant throughout the problem; indicating that energy is conserved, and agrees well with results published in the literature (Zhang et al. 2007; Paulino et al. 2010).

We also investigate the effect that microstructural heterogeneities might have on the global fracture patterns, by varying the bulk elastic modulus, the cohesive fracture energy and the cohesive strength as discussed in Sect. 4. The study was conducted on the coarse polygonal mesh, the coarse polygonal mesh with element splitting and the adaptively refined coarse polygonal mesh. For each material property considered, three different Weibull moduli were selected, $m = 10, 30,$ and 50, and for each Weibull modulus three different random instances were simulated. Based on the study,

statistically distributing the material properties does not have a noticeable effect on the global fracture patterns. For sake of brevity, not all of the results are shown here, but typical results are illustrated in Fig. 29. We illustrate the two meshes in most need of improvement, coarse polygonal meshes with and without element splitting, with the widest variation of material properties ($m = 10$) for each property we consider. From the results, it is clear that using a statistical distribution of material properties to overcome mesh dependency does not significantly improve the global fracture patterns for the geometrically restrictive polygonal meshes. For the element splitting case, with a variation in cohesive strength (Fig. 29f), the frequency of microbranching increases.

In addition to the global fracture patterns, we investigate the effect that microstructural heterogeneities have on the crack tip velocity. The same scenarios as in the fracture pattern investigation are considered, and the average crack tip velocities are summarized in Table 3. Because the crack tip velocity fluctuates significantly while the crack propagates, the average velocity is only representative of the overall trend and should not be taken as a precise value. While the tabulated velocities all fall within the expected range observed experimentally (Sharon and Fineberg 1996), the coarse polygonal mesh consistently produces the slowest velocity, and the adaptively refined mesh consistently produces the fastest velocity. There is no observable influence of the statistical distribution of material properties.
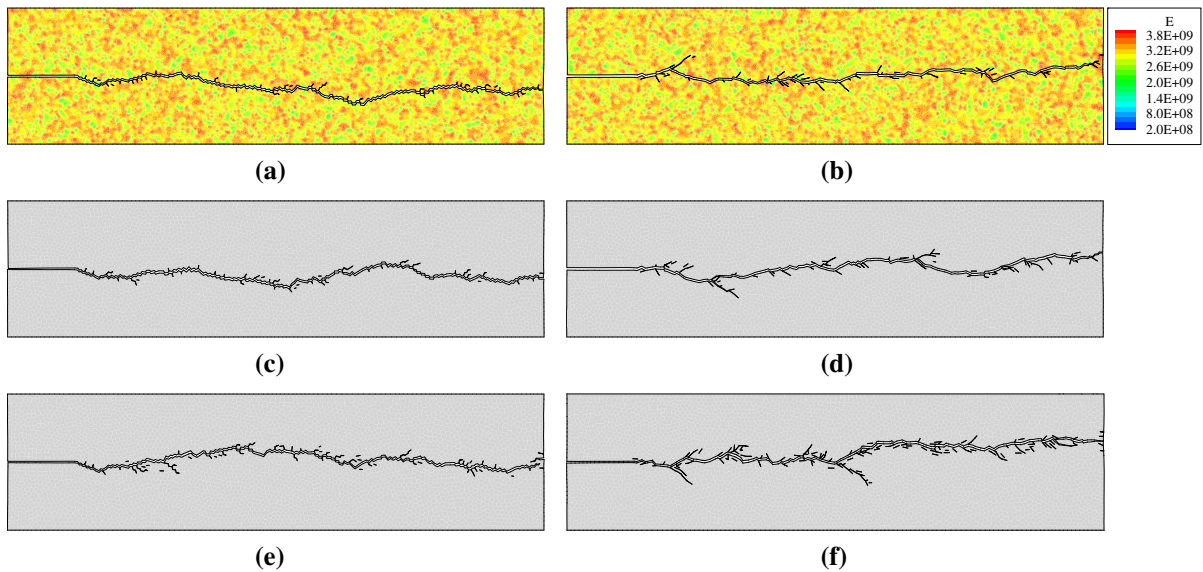
Fig. 29 Global fracture patterns for the microbranching problem when the material is statistically distributed. Results are for: **a**, **b** a variation in elastic modulus for the case of a coarse polygonal mesh without element splitting and with element splitting, respectively; **c**, **d** a variation in cohesive energy (140 N/m $\leq \phi_n \leq$ 440 N/m) for the same cases, respectively; and **e**, **f** a variation in cohesive strength (55 MPa $\leq \sigma_n \leq$ 162 MPa) for the same cases, respectively. Results are shown for a Weibull modulus of $m = 10$, but illustrate the minor effect that the materially unstructured method has on global fracture patterns when using unstructured polygonal elements

Table 3 Summary of average crack tip velocity when material is statistically distributed

	Distribution of Material			
	Homogeneous	$m = 50$	$m = 30$	$m = 10$
Coarse Polygonal				
Cohesive Stress (σ)		562	547	547
Cohesive Energy (ϕ)	543	557	531	551
Elastic Modulus (E)		533	521	504
Element Splitting				
Cohesive Stress (σ)		630	624	638
Cohesive Energy (ϕ)	597	582	594	605
Elastic Modulus (E)		607	589	605
Adaptive Refinement				
Cohesive Stress (σ)		681	662	689
Cohesive Energy (ϕ)	667	677	682	673
Elastic Modulus (E)		654	669	650

Results are averaged over three different random instances and are listed in units of meters per second (m/s)

The computational time is listed in Table 4. Similarly to the double notched plate example, the number of iterations it takes for the specimen to fracture completely, depends on the meshing strategy. The total cost is lowest for the adaptively refined coarse polygonal mesh, and highest for the fine polygonal mesh.

Alternatively, when considering the cost per iteration, the coarse polygonal mesh becomes the lowest cost option. Once again, this is in line with expectations, as the adaptively refined mesh adds elements and nodes to the problem as the simulation progresses. Computations using an adaptive refinement scheme, as opposed

Table 4 Summary of computational cost to simulate the various cases considered for the microbranching example

Case	Elements	Nodes	Cost (min)	Iterations to fracture	Cost/iteration (ms)
1	4,000	7,188	21.5	28,200	45.7
2	4,000	7,188	20.8	23,000	54.3
3	**4,000**	**7,188**	**19.1**	**21,000**	**54.6**
4	22,039	43,538	116.8	25,200	278.1
5	22,039	22,375	56.0	22,400	150.0

The five cases correspond to: (1) a coarse polygonal mesh, (2) a coarse polygonal mesh with element splitting, (3) an adaptively refined coarse polygonal mesh with element splitting (the final mesh contains 9,395 elements and 12,436 nodes), (4) a fine polygonal mesh, and (5) a fine quadrilateral mesh with element splitting. The elements and nodes correspond to the initial discretization (the base mesh), and the wall-clock time is recorded in minutes. The time step was held constant at $\Delta t = 1 \times 10^{-9} \, \mu$s. The bold values correspond to the newly proposed adaptive refinement scheme

to a uniformly refined mesh of the same effective discretization, produce comparable results and are almost three times faster.

6 Concluding remarks

Unstructured polygonal meshes are isotropic, showing no bias to fracture patterns, but have limited fracture paths due to the small number of degrees present at each node. By applying an adaptive mesh refinement scheme which is designed to increase the number of paths on which a crack may travel, in dynamic fracture simulations, the geometric restrictions present in polygonal meshes can be alleviated. We present a conforming refinement scheme targeted at unstructured polygonal meshes. The scheme consists of subdividing each polygonal element into unstructured quadrilateral elements. In addition, we combine the refinement scheme with an element splitting procedure (Leon et al. 2014).

The geometrical representation of crack length, and deviation is investigated through a probabilistic series of mesh quality studies. The refinement scheme is compared with unrefined polygonal meshes, both with and without element splitting. The investigation quantifies the ability of the refined mesh to represent arbitrary fracture patterns with minimal error. We address the use of geometrically and topologically unstructured means for addressing mesh dependency, together with the use of materially unstructured means. The materially unstructured method is investigated in the example problems by statistically distributing the primary bulk and cohesive material properties, and investigating the effects they have on the global fracture patterns and

crack tip velocities. Our investigation shows that the effects are minor and almost negligible when compared to the improvements demonstrated by the geometric refinement scheme.

The numerical methods are verified with three example problems, which are supported with experimental results from the literature. The three examples cover mode I, mixed-mode, and microbranching behavior. The mixed-mode problems illustrate the improvements that the adaptive refinement scheme presents in capturing both crack initiation angles and global fracture patterns. Both the crack tip velocity and the evolution of energy are computed and compare well with experimental and numerical results published in the literature. The microbranching behavior, observed experimentally, is also captured when using the geometric and topological strategies proposed in this paper. In addition to showing improved capabilities in capturing fracture behavior, the adaptive refinement scheme is shown to be computationally advantageous. The cost per iteration for the adaptive refinement scheme is shown to be only slightly higher than that for a coarse polygonal mesh.

In this paper, we focus on the unique geometric characteristics of polygonal elements for reducing mesh induced restrictions to crack propagation. However, we note that there is room for the extensions of this work. For example, adaptive refinement of unstructured polygonal meshes, with the cohesive element framework, could allow one to bridge length scales in hierarchical materials. The fine scale features of a hierarchical material can be captured with the adaptive refinement technique detailed here, while the coarse regions of the mesh could be used to represent the homoge-

nized response of the bulk material. Heterogeneity in the bulk material has been treated in this work with a simplified statistical distribution for nearly homogeneous materials, but the unstructured polygonal elements provide flexibility in representing distributions of heterogeneity in a material. For example, at small scales, the polygonal elements could represent grains in metals and alloys, while the adaptive refinement and splitting could be used to represent either intergranular or intragranular fracture, see Fig. 1.

References

Babuška I, Rheinboldt WC (1978) A-posteriori error estimates for the finite element method. Int J Numer Methods Eng 12:1597–1615

Bathe KJ (1996) Finite element procedures. Prentice Hall, Prentice

Belytschko T, Black T (1999) Elastic crack growth in finite elements with minimal remeshing. Int J Numer Methods Eng 45:601–620

Belytschko T, Chen H, Xu J, Zi G (2003) Dynamic crack propagation based on loss of hyperbolicity and a new discontinuous enrichment. Int J Numer Methods Eng 58:1873–1905

Bishop JE, Martinez MJ, Newell P (2012) A finite-element method for modeling fluid-pressure induced discrete-fracture propagation using random meshes. 46th US Rock Mechanics/Geomechanics Symposium

Bishop JE (2009) Simulating the pervasive fracture of materials and structures using randomly close packed Voronoi tessellations. Comput Mech 44:455–471

Blal N, Daridon L, Monerie Y, Pagano S (2012) Artificial compliance inherent to the intrinsic cohesive zone models: criteria and application to planar meshes. Int J Fract 178:71–83

Bolander JE, Saito S (1998) Fracture analyses using spring networks with random geometry. Eng Fract Mech 61:569–591

Celes W, Paulino GH, Espinha R (2005a) A compact adjacency-based topological data structure for finite element mesh representation. Int J Numer Methods Eng 64:1529–1556

Celes W, Paulino GH, Espinha R (2005b) Efficient handling of implicit entities in reduced mesh representations. J Comput Inf Sci Eng 5:348–359

Cerrone A, Wawrzynek P, Nonn A, Paulino GH, Ingraffea A (2014) Implementation and verification of the Park–Paulino–Roesler cohesive zone model in 3D. Eng Fract Mech. doi:10.1016/j.engfracmesh.2014.03.010

Dijkstra EW (1959) A note on two problems in connexion with graphs. Numer Math 1:269–271

Fries TP, Zilian A (2009) On time integration in the XFEM. Int J Numer Methods Eng 78:69–93

Grätsch T, Klaus-Jürgen B (2005) A posteriori error estimation techniques in practical finite element analysis. Comput Struct 83:235–265

Gravouil A, Elguedj T, Maigre H (2009) An explicit dynamics extended finite element method. Part 2: element-by-element stable-explicit/explicit dynamic scheme. Comput Methods Appl Mech Eng 198:2318–2328

Grégoire D, Maigre H, Réthoré J, Combescure A (2007) Dynamic crack propagation under mixed-mode loading—comparison between experiments and X-FEM simulations. Int J Solids Struct 44:6517–6534

Hopkinson B (1914) A method of measuring the pressure produced in the detonation of high explosives or by the impact of bullets. Proc R Soc A Math Phys Eng Sci 89(612):411–413

Hu C, Ghosh S (2008) Locally enhanced Voronoi cell finite element model (LE-VCFEM) for simulating evolving fracture in ductile microstructures containing inclusions. Int J Numer Methods Eng 76:1955–1992

Huttenlocher DP, Klanderman GA, Rucklidge WJ (1993) Comparing images using the Hausdorff distance. IEEE Trans Pattern Anal Mach Intell 15:850–863

Kalthoff JF, Winkler S (1987) Failure mode transition at high rates of shear loading. Int Conf Impact Load Dyn Behav Mater 1:185–195

Khoei AR, Azadi H, Moslemi H (2008) Modeling of crack propagation via an adaptive mesh refinement based on modified superconvergent patch recovery technique. Eng Fract Mech 75:2921–2945

Klein PA, Foulk JW, Chen EP, Wimmer SA, Gao H (2000) Physics-based modeling of brittle fracture: Cohesive formulations and the application of meshfree methods. Technical Report, Sandia National Laboratories

Leon SE, Spring DW, Paulino GH (2014) Reduction in mesh bias for dynamic fracture using adaptive splitting of polygonal finite elements. Int J Numer Methods Eng 1–23

Li S, Ghosh S (2006a) Multiple cohesive crack growth in brittle materials by the extended voronoi cell finite element model. Int J Fract 141:373–393

Li S, Ghosh S (2006b) Extended voronoi cell finite element model for multiple cohesive crack propagation in brittle materials. Int J Numer Methods Eng 65:1028–1067

Lloyd SP (1982) Least squares quantization in PCM. IEEE Trans Inf Theory 28:129–137

Miller O, Freund LB, Needleman A (1999) Energy dissipation in dynamic fracture of brittle materials. Model Simul Mater Sci Eng 6:607–638

Molinari JF, Ortiz M (2002) Three-dimensional adaptive meshing by subdivision and edge-collapse in finite-deformation dynamic-plasticity problems with application to adiabatic shear banding. Int J Numer Methods Eng 53:1101–1126

Mota A, Sun W, Ostien JT, Foulk JW, Long KN (2013) Lie-group interpolation and variational recovery for internal variables. Comput Mech 52:1281–1299

Ooi ET, Song C, Tin-Loi F, Yang Z (2012a) Polygon scaled boundary finite elements for crack propagation modelling. Int J Numer Methods Eng 91:319–342

Ooi ET, Shi M, Song C, Tin-Loi F (2012b) Automatic dynamic crack propagation modeling using polygon scaled boundary finite elements, chap 65. CRC Press, Boca Raton

Ooi ET, Shi M, Song C, Tin-Loi F, Yang ZJ (2013) Dynamic crack propagation simulation with scaled boundary polygon elements and automatic remeshing technique. Eng Fract Mech 106:1–21

Ortiz M, Pandolfi A (1999) Finite-deformation irreversible cohesive elements for three-dimensional crack-propagation analysis. Int J Numer Methods Eng 44:1267–1282

Park K, Pereira J, Duarte CA, Paulino GH (2009) Integration of singular enrichment functions in the generalized/extended finite element method for three-dimensional problems. Int J Numer Methods Eng 78:1220–1257

Park K, Paulino GH, Roesler JR (2009) A unified potential-based cohesive model for mixed-mode fracture. J Mech Phys Solids 57:891–908

Park K, Paulino GH, Celes W, Espinha R (2012) Adaptive mesh refinement and coarsening for cohesive zone modeling of dynamic fracture. Int J Numer Methods Eng 92:1–35

Paulino GH, Menezes IFM, Neto JBC, Martha LFRC (1999) A methodology and adaptive finite element analysis: towards an integrated computational environment. Comput Mech 23:361–388

Paulino GH, Celes W, Espinha R, Zhang ZJ (2008) A general topology-based framework for adaptive insertion of cohesive elements in finite element meshes. Eng Comput 24:59–78

Paulino GH, Park K, Celes W, Espinha R (2010) Adaptive dynamic cohesive fracture simulations using nodal perturbation and edge-swap operators. Int J Numer Methods Eng 84:1303–1343

Remmers JJC, de Borst R, Needleman A (2008) The simulation of dynamic crack propagation using the cohesive segments method. J Mech Phys Solids 56:70–92

Rimoli JJ, Rojas JJ (2013) Meshing strategies for the alleviation of mesh-induced effects in cohesive element models. arXiv preprint arXiv:13021162

Rimoli JJ, Rojas JJ, Khemani FN (2012) On the mesh dependency of cohesive zone models for crack propagation analysis. In: 53rd AIAA/ASME/ASCE/AHS/ASC structure, structural dynamics and materials conference, American Institute of Aeronautics and Astronautics

Rockafellar RT, Wets RJB, Wets M (1998) Variational analysis, vol 317. Springer, Berlin

Sharon E, Gross SP, Fineberg J (1995) Local crack branching as a mechanism for instability in dynamic fracture. Phys Rev Lett 74:5096–5099

Sharon E, Fineberg J (1996) Microbranching instability and the dynamic fracture of brittle materials. Phys Rev B 54:7128–7139

Strouboulis T, Babuška I, Copps K (2000) The design and analysis of the generalized finite element method. Comput Methods Appl Mech Eng 181:43–69

Strouboulis T, Copps K, Babuška I (2001) The generalized finite element method. Comput Methods Appl Mech Eng 190:4081–4193

Sukumar N, Malsch EA (2006) Recent advances in the construction of polygon finite element interpolants. Arch Comput Methods Eng 13:129–163

Talischi C, Paulino GH, Periera A, Menezes IFM (2012) Polymesher: a general-purpose mesh generator for polygonal elements written in Matlab. J Struct Multidiscip Optim 45:309–328

Talischi C, Paulino GH, Pereira A, Menezes IFM (2012) Polytop: a Matlab implementation of a general topology optimization framework using unstructured polygonal finite element meshes. J Struct Multidiscip Optim 3:329–357

Velho L, Gomes J (2000) Variable resolution 4-k meshes: concepts and applications. Comput Graphics Forum 19:195–212

Wachspress EL (1975) A rational finite element basis. Academic Press, New York

Weibull W (1939) A statistical theory of the strength of materials. Proc R Acad Eng Sci 151:1–45

Zhang Z, Paulino GH, Celes W (2007) Extrinsic cohesive zone modeling of dynamic fracture and microbranching instability in brittle materials. Int J Numer Methods Eng 72:893–923

Zhang Z, Paulino GH (2005) Cohesive zone modeling of dynamic failure in homogeneous and functionally graded materials. Int J Plast, special issue on "Inelastic Response of Multiphase Materials" 21:1195–1254

Zhou F, Molinari JF (2004) Dynamic crack propagation with cohesive elements: a method to address mesh dependency. Int J Numer Methods Eng 59:1–24

Zienkiewicz OC, Zhu JZ (1992a) The superconvergent patch recovery and a posteriori error estimates. Part 1: the recovery technique. Int J Numer Methods Eng 33:1331–1364

Zienkiewicz OC, Zhu JZ (1992b) The superconvergent patch recovery and a posteriori error estimates. Part 2: error estimates and adaptivity. Int J Numer Methods Eng 33:1365–1382